

10

Physical Model Technique for Design of Robotic Manipulators in Manufacturing Systems

- 10.1. [Introduction](#)
- 10.2. [Technique of Physical Models of Solution Space for Robotic Manipulators](#)
Model of Solution Space for 3-DOF Delta Parallel Robots •
Model of Solution Space for F/T Sensors Based on Stewart Platform
- 10.3. [Performance Evaluation Criteria for Design of Robotic Mechanisms](#)
Three Kinds of Workspaces • Three Kinds of Singularities •
Global Conditioning Index • Global Velocity Index • Global Payload Index • Global Deformation Index • Global Error Index
- 10.4. [Performance Atlases for Design of Serial Robots with Three Moving Links](#)
Robotic Principle Motion • Atlases of Workspace Criteria • Atlas of Global Conditioning Index • Global Workspace Atlas •
Atlases of Global Velocity Index • Atlases of Global Payload Index • Atlases of Global Deformation Index • Distribution of Commercial Robots on the Solution Space Model
- 10.5. [Atlases for Design of F/T Sensor Based on Stewart Platform](#)
- 10.6. [Conclusions](#)

Feng Gao

Hebei University of Technology

10.1 Introduction

The mechanical design of industrial robots requires the application of engineering expertise in a variety of areas. Important disciplines include machine design, structure design, and mechanical, control, and electrical engineering. Traditionally, mechanism design has been based largely on use of specifications including number of axes, workspace volume, payload capacity, and end-effector speed. Robots have not been designed to perform specific tasks but to meet general performance criteria.

In the design of industrial robots, the design of the robotic mechanisms is one of the most important activities because these mechanisms determine the performance characteristics of the robotic machines.

Although some methods and criteria have been developed for robotic mechanism design and many types of robotic mechanisms have been proposed, there has not been a unified method for the design.

One reason for this is that there has not been a method to visualize the performance characteristics of robots and many criteria just show the local performance characteristics of robots.

In this chapter, a novel method of the physical model technique for the design of robotic mechanisms is introduced. We establish several kinds of physical models of solution space for serial and parallel robots [1-9]; propose many important global performance criteria for evaluation of robotic mechanisms; and utilize the physical model technique and performance criteria to construct the performance atlases of robotic mechanisms which are used to analyze the relationships between the performance criteria and link lengths of robotic mechanisms. The performance atlases are a very efficient and useful tool for design of robotic mechanisms.

10.2 Technique of Physical Models of Solution Space for Robotic Manipulators

As you know, link lengths of robotic mechanisms may vary between zero and infinity. This means that links can be very long or short and can be measured by different units or unit systems (such as meter, millimeter, foot, and inch). It is very difficult to investigate the relationship between the performance criteria and link lengths of all the robots. Therefore, it is convenient to eliminate the physical sizes of the robotic mechanisms to investigate the robotic design method.

Model of Solution Space for Robots with Three Moving Links

Human arms, legs, and fingers, and limbs of animals and insects can be viewed as mechanisms with three moving links. Fingers of dextrous hands [10–22], arms of industrial robots [23–27, 32–35], and legs of walking machines [28–30] often consist of three moving links. Therefore, an understanding of the relationships between the criteria and the dimensions of three-moving-link mechanisms is of great importance for design of fingers, arms, and legs of robotic machines. The robotic mechanisms with three moving links can be used for 3-, 4-, ..., 7-DOF serial robots, as shown in Fig. 10.1. For example, if joints A, B, and C are revolute pairs, it can be viewed as a 3-DOF robotic mechanism. When joints A and C are spherical pairs and joint B is a revolute pair, they comprise a 7-DOF redundant spatial robotic mechanism. Therefore, to investigate the robotic mechanisms with three moving links has generality.

Because the link lengths may have a wide range of possible values, it is convenient to avoid explicit use of the physical sizes of the mechanisms during analysis and design. We shall define normalized parameters of the mechanisms and construct a physical model of the solution space as follows.

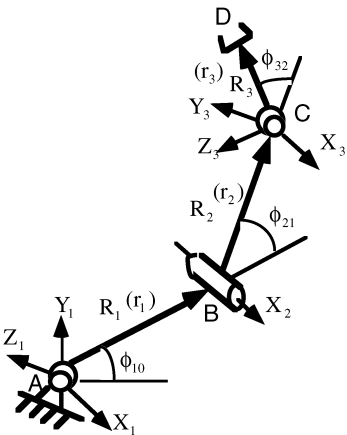


FIGURE 10.1 A serial robotic mechanism with three moving links. (a) 3-D model, (b) 2-D model with 3 coordinates.

To facilitate the analysis, we normalize the parameters of a serial mechanism as shown in Fig. 10.1 If the link lengths of the mechanism are R_i ($i = 1, 2$, and 3), we define

$$r_i = R_i / L; \quad i = 1, 2, \text{ and } 3 \tag{10.1}$$

$$L = (R_1 + R_2 + R_3) / 3 \tag{10.2}$$

where, r_i is the nondimensional parameter of the robotic mechanisms with three moving links. From Eqs. (10.1) and (10.2), we obtain:

$$r_1 + r_2 + r_3 = 3 \tag{10.3}$$

$$0 \leq r_i \leq 3, \quad i = 1, 2, \text{ and } 3. \tag{10.4}$$

Let r_1 , r_2 , and r_3 be orthogonal coordinate axes. Using Eqs. (10.3) and (10.4), we generate a physical model of the solution space, as shown in Fig. 10.2, consisting of an equilateral triangle ABC for which any possible combination of the link lengths is represented by r_1 , r_2 , and r_3 . The resulting model graphically provides a means to represent all possible mechanisms with three moving links. In this model, points A, B, and C have coordinates (3, 0, 0), (0, 3, 0), and (0, 0, 3), respectively; then edges BC, AB, and AC satisfy conditions $r_1 = 0$, $r_2 = 0$, and $r_3 = 0$, respectively. Within triangle ABC, we inscribe another equilateral triangle EFG, where edges EG, FG, and EF satisfy $r_1 = r_2 + r_3$, $r_2 = r_1 + r_3$, and, $r_3 = r_1 + r_2$, respectively (as shown in Fig. 10.2(b)). Triangle EFG divides triangle ABC into regions I, II, III, and IV. Table 10.1 describes the geometric characteristics of the four classes of mechanisms.

By using the solution space model, we can investigate relationships between performance criteria and link lengths of the robotic mechanisms.

TABLE 10.1 Dimensional Properties of Mechanisms with Three Moving Links

Region	Dimensional Characteristics	Distribution
I	$r_1 > r_2 + r_3$	ΔAEG
II	$r_2 > r_1 + r_3$	ΔFGC
III	$r_3 > r_1 + r_2$	ΔBEF
IV	$r_1 \leq r_2 + r_3 \cap r_2 \leq r_1 + r_3 \cap r_3 \leq r_1 + r_2$	ΔEFG

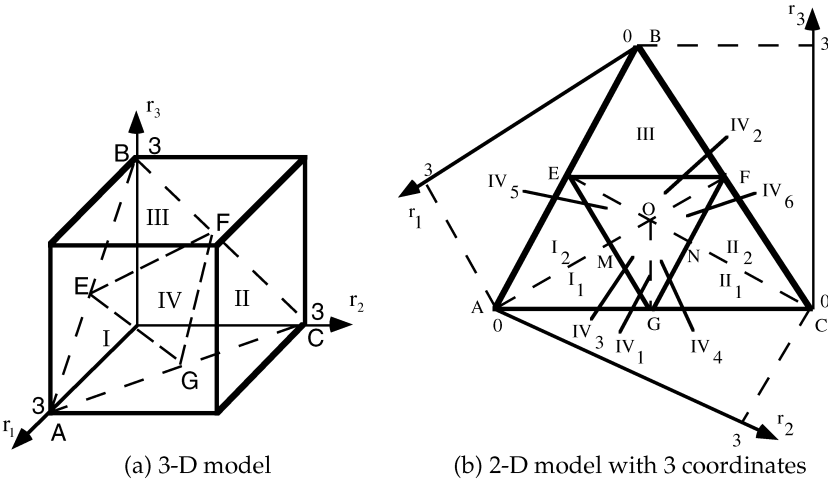


FIGURE 10.2 Model of solution space for mechanisms with three moving links.

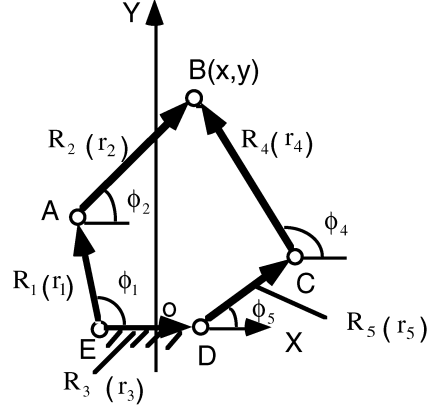


FIGURE 10.3 A typical 2-DOF PPM. (a) 3-D model, (b) 2-D model with 3 coordinates.

Model of Solution Space for 2-DOF Parallel Planar Manipulators

Since parallel robots have advantages, compared with serial robots (i.e., their stiffness, speed, payload, and precision are higher), much research has been devoted to them.

2-DOF parallel-planar manipulators (PPMs) are an important class of robotic manipulators that can follow an arbitrary planar curve. Because of their usefulness in applications, these mechanisms have attracted the attention of researchers who have investigated their workspace, mobility, and methods for analysis and design [36–42].

Although much research has been devoted to 2-DOF PPMs, there has not been a study of the relationships between the criteria and link lengths of 2-DOF PPMs. The reason for this is that there has not been an effective method to solve the problem.

Figure 10.3 shows a typical 2-DOF PPM. Since any of the actual link lengths of the manipulator lies in the range zero to infinity, we have to eliminate the physical size of the manipulator from the discussion. Let:

$$r_i = R_i / L \quad (i = 1, 2, 3, \dots, 5) \quad (10.5)$$

where R_i is the actual length of link i and r_i is the nondimensional relative length of link i . And

$$L = \frac{1}{4} \sum_{i=1}^5 R_i \quad (10.6)$$

where L is the average length of all links for the manipulator. Gosselin [31] has shown that the parallel manipulator should be symmetric, so that we have the following results:

$$R_5 = R_1 \quad \text{and} \quad R_4 = R_2; \quad r_5 = r_1 \quad \text{and} \quad r_4 = r_2 \quad (10.7)$$

These conditions show us that the two input links should have the same length and the two coupling bars also have the same length. Therefore, the sum of the five link lengths is

$$2r_1 + 2r_2 = r_3 = 4 \quad (10.8)$$

If the manipulator can be assembled, the range of the relative link lengths should be 0 to 2, so

$$0 < r_i < 2 \quad (i = 1, 2, 4, 5) \quad \text{and} \quad 0 \leq r_3 < 2 \quad (10.9)$$

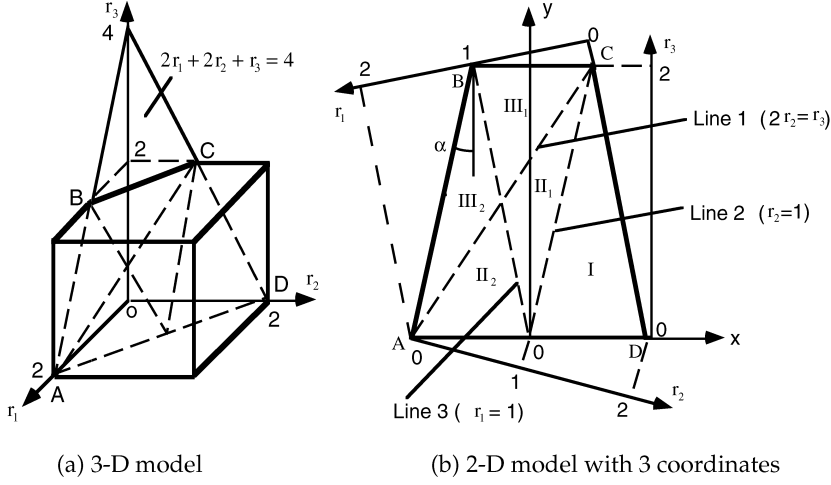


FIGURE 10.4 Model of the solution space for 2-DOF PPMs.

Using these equations and inequalities, the model of the solution space for 2-DOF PPMs can be constructed as shown in Fig. 10.4(a), which is an isosceles trapezoid ABCD. Within the model, all 2-DOF PPMs can exist and the relationships between the different criteria and dimensions of the manipulators can be investigated.

For convenience, the model of the solution space, which is an isosceles trapezoid ABCD in the $r_1 r_2 r_3$ coordinate system as shown in Fig. 10.4(a) can be changed into the isosceles trapezoid ABCD in the xy coordinate system as shown in Fig. 10.4(b), by using the following equations:

$$\begin{pmatrix} x \\ y \end{pmatrix} = \begin{pmatrix} 1/\cos\alpha \\ 0 \end{pmatrix} - \begin{bmatrix} 1/\cos\alpha & 1/(4\cos\alpha) \\ 0 & -1 \end{bmatrix} \begin{pmatrix} r_1 \\ r_3 \end{pmatrix} \quad (10.10)$$

where

$$\alpha = \sin^{-1} 1/4$$

When the input links r_1 and r_5 are located at the extreme positions and the angular velocities $\dot{\phi}_2$ and $\dot{\phi}_4$ are not equal to zero, the angular velocities $\dot{\phi}_1$ and $\dot{\phi}_5$ must be equal to zero, that is

$$\dot{\phi}_1 = 0 \quad \text{and} \quad \dot{\phi}_5 = 0 \quad (10.11)$$

From Eqs. 10.7, 10.8, and 10.11,

$$\begin{pmatrix} \dot{\phi}_1 \\ \dot{\phi}_5 \end{pmatrix} = \frac{1}{r_1 r_5 \sin(\phi_1 - \phi_5)} \begin{bmatrix} r_2 r_5 \sin(\phi_5 - \phi_2) & r_4 r_5 \sin(\phi_4 - \phi_5) \\ r_1 r_2 \sin(\phi_1 - \phi_2) & r_1 r_4 \sin(\phi_4 - \phi_1) \end{bmatrix} \begin{pmatrix} \dot{\phi}_2 \\ \dot{\phi}_4 \end{pmatrix}$$

we can derive three conditions:

$$\text{Line 1:} \quad 2r_2 = r_3 \quad (10.12)$$

$$\text{Line 2:} \quad 2r_2 = 2r_1 + r_3 \quad \text{or} \quad r_2 = 1 \quad (10.13)$$

$$\text{Line 3:} \quad 2r_1 = 2r_2 + r_3 \quad \text{or} \quad r_1 = 1 \quad (10.14)$$

Using Eqs. (10.12), (10.13), and (10.14), three lines can be drawn on the model of solution space, which divide the model into five regions I, II₁, II₂, III₁, and III₂, as shown in Fig. 10.4(b). By analyzing the characteristics of the mechanisms in the five regions, respectively, the mechanisms can be classified as four types, as shown in Table 10.2.

In Table 10.2, we define

- UDCM = Unrestrained double crank 2-DOF PPMs;
- RDCM = Restrained double crank 2-DOF PPMs;
- DRM = Double rocker 2-DOF PPMs;
- CPM = Change point 2-DOF PPMs.

Model of Solution Space for 3-DOF Parallel Planar Manipulators

Since 3-DOF parallel planar manipulators (PPMs) can follow both an arbitrary planar curve and an orientation, they are an important class of robotic manipulators. Figure 10.5 shows a typical 3-DOF PPM. Since any of the actual link lengths of the manipulator lies in the range zero to infinity, we have to eliminate the physical size of the manipulator from the discussion.

Nondimensional Parameters of 3-DOF PPMs

Let

$$r_i = R_i / L \quad (i = 1, 2, 3, \dots, 12) \tag{10.15}$$

TABLE 10.2 Complete Classification of 2-DOF PPMs

Type No.	Region	Symbol of Type	Dimensional Characteristics
1	I	UDCM	$r_2 > 1$
2	II ₁	RDCM	$r_2 < 1 \cap r_1 < 1 \cap 2r_2 > r_3$
	II ₂	RDCM	$2r_2 > r_3 \cap r_1 > 1$
3	III ₁	DRM	$2r_2 < r_3 \cap r_1 < 1$
	III ₂	DRM	$2r_2 < r_3 \cap r_1 > 1$
4	Line 1	CPM	$2r_2 = r_3$
	Line 2	CPM	$2r_2 = 2r_1 + r_3 \quad \text{or} \quad r_2 = 1$
	Line 3	CPM	$2r_1 = 2r_2 + r_3 \quad \text{or} \quad r_1 = 1$

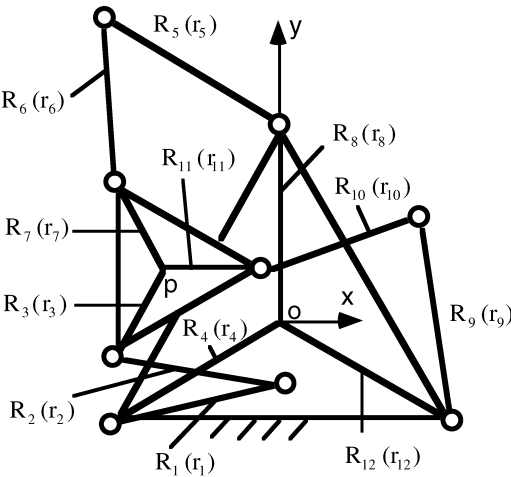


FIGURE 10.5 A typical 3-DOF PPM.

where R_i is the actual length of link i and r_i is the nondimensional relative length of link i . And

$$L = \frac{1}{12} \sum_{i=1}^{12} R_i \quad (10.16)$$

where L is the average length of all links for the manipulator. Gosselin [31] has shown that the parallel manipulator should be symmetric, so that we have the following results:

$$\begin{array}{ll} R_9 = R_5 = R_1 & r_9 = r_5 = r_1 \\ R_{10} = R_6 = R_2 & r_{10} = r_6 = r_2 \\ R_{11} = R_7 = R_3 & r_{11} = r_7 = r_3 \\ R_{12} = R_8 = R_4 & r_{12} = r_8 = r_4 \end{array} \quad \text{and} \quad (10.17)$$

Therefore, only four parameters (r_1, r_2, r_3 , and r_4) are needed to consider. From Eqs. (10.15), (10.16), and (10.17), we see that the sum of the 12 nondimensional relative link lengths is

$$r_1 + r_2 + r_3 + r_4 = 4 \quad (10.18)$$

Model of Solution Space for 3-DOF PPMs

If the manipulator can be assembled, the range of the nondimensional relative link lengths should be 0 to 2, so

$$0 < r_i < 2 \quad (i = 1, 2, \dots, 12) \quad (10.19)$$

Using these equations and inequalities, the model of the solution space for 3-DOF PPMs can be constructed, which is an irregular octahedron ABCDEF as shown in Fig. 10.6. Within the model, all 3-DOF PPMs can exist and the relationships between the different criteria and dimensions of the manipulators can be investigated.

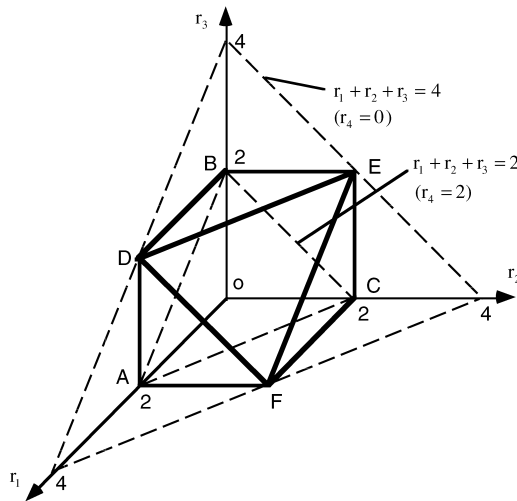


FIGURE 10.6 The physical model of the solution space for 3-DOF PPMs. (a) $r_4 = 0$, (b) $0 < r_4 < 1$, (c) $r_4 = 1$, (d) $1 < r_4 < 2$, (e) $r_4 = 2$.

Planar Closed Configurations with Coordinates $r_1 r_2 r_3$

When r_4 takes several values (such as 0, 0.2, 0.4, 0.6, 0.8, 1.0,..., 1.8), a set of plane equations can be obtained by means of Eq. 10.18. Therefore, r_4 is an auxiliary coordinate axis in the model of the solution space. When taking $r_4 = 0, 0 < r_4 < 1, r_4 = 1, 1 < r_4 < 2$, and $r_4 = 2$, respectively, five types of planar closed configurations with the three coordinates $r_1 r_2 r_3$ are obtained (as shown in Fig. 10.7). When $r_4 = 2$, the mechanisms have no motion.

As shown in Fig. 10.8, a planar closed configuration has three coordinates $r_1 r_2 r_3$. Since only two of them are independent in a plane, we can use two orthogonal coordinates $x y$ to express $r_1 r_2 r_3$ by using the following equations. When r_1, r_2 , and r_3 are given, we can calculate coordinates x and y from Eq. (10.20). When x and y are given, we can calculate r_1, r_2 , and r_3 from Eq. (10.21).

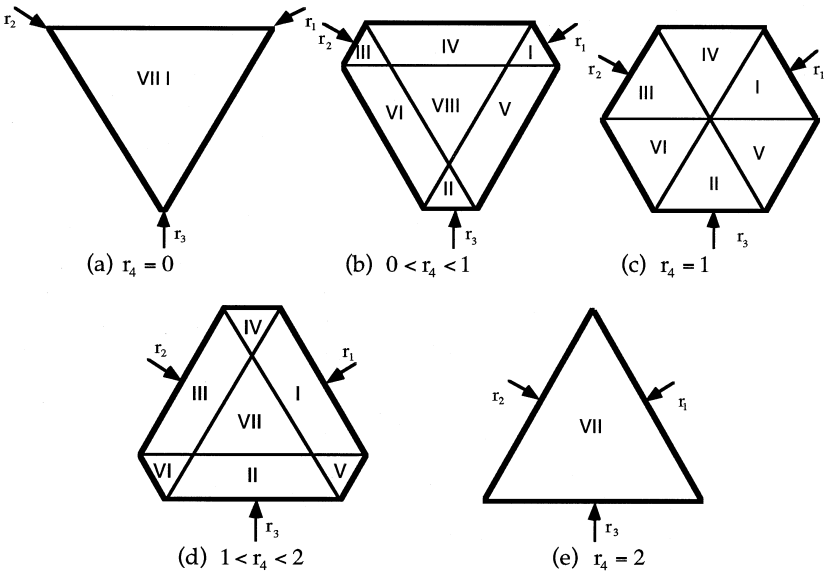


FIGURE 10.7 Five types of planar closed configurations.

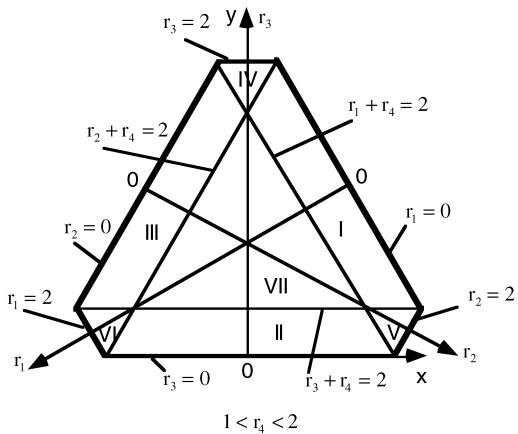


FIGURE 10.8 The coordinate transformation.

The Eqs. (10.20) and (10.21) are useful for constructing the performance atlases within the planar closed configurations.

$$\begin{pmatrix} x \\ y \end{pmatrix} = \begin{bmatrix} -\sqrt{3}/3 & \sqrt{3}/3 & 0 \\ 0 & 0 & 1 \end{bmatrix} \begin{pmatrix} r_1 \\ r_2 \\ r_3 \end{pmatrix} \quad (10.20)$$

$$\begin{pmatrix} r_1 \\ r_2 \\ r_3 \end{pmatrix} = \begin{bmatrix} -\sqrt{3}/2 & -1/2 & 2 - r_4/2 \\ \sqrt{3}/2 & -1/2 & 2 - r_4/2 \\ 0 & 1 & 0 \end{bmatrix} \begin{pmatrix} x \\ y \\ 1 \end{pmatrix} \quad (10.21)$$

Classification of all 3-DOF PPMs

Among the four links, r_1 , r_2 , r_3 , and r_4 in a 3-DOF PPM, when the sum of any two link lengths is equal to the sum of the other two link lengths, it is designated as a change point 3-DOF PPM. Physically, it means that all four links (r_1 , r_2 , r_3 , and r_4) can be collinear. According to the definition of change point 3-DOF PPM, we yield the conditions that express three kinds of change point 3-DOF PPMs as follows:

$$r_1 + r_4 = r_2 + r_3 = 2 \quad (10.22)$$

$$r_2 + r_4 = r_1 + r_3 = 2 \quad (10.23)$$

$$r_3 + r_4 = r_1 + r_2 = 2 \quad (10.24)$$

The Eqs. (10.22), (10.23), and (10.24) can define three planes, respectively. By using the three planes, the model of the solution space as shown in Fig. 10.6 can be divided into eight parts. Within the planar closed configurations, Eqs. (10.22), (10.23), and (10.24) express three lines (as shown in Figs. 10.7 and 10.8), which partition the planar closed configurations into eight regions I, II, III, IV, V, VI, VII, and VIII. Each region defines a type of 3-DOF PPMs. According to analysis of the dimensional characteristics of the 3-DOF PPMs within the regions I~VIII, the inequalities Eqs. (10.25)–(10.32) can be derived.

$$r_1 + r_2 < r_3 + r_4 \cap r_1 + r_3 < r_2 + r_4 \cap r_1 + r_4 < r_2 + r_3 \quad (10.25)$$

$$r_2 + r_1 < r_3 + r_4 \cap r_2 + r_3 < r_1 + r_4 \cap r_2 + r_4 < r_1 + r_3 \quad (10.26)$$

$$r_3 + r_1 < r_2 + r_4 \cap r_3 + r_2 < r_1 + r_4 \cap r_3 + r_4 < r_1 + r_2 \quad (10.27)$$

$$r_3 + r_1 > r_2 + r_4 \cap r_3 + r_2 < r_1 + r_4 \cap r_3 + r_4 > r_1 + r_2 \quad (10.28)$$

$$r_2 + r_1 > r_3 + r_4 \cap r_2 + r_3 < r_1 + r_4 \cap r_2 + r_4 > r_1 + r_3 \quad (10.29)$$

$$r_1 + r_2 > r_3 + r_4 \cap r_1 + r_3 < r_2 + r_4 \cap r_1 + r_4 > r_2 + r_3 \quad (10.30)$$

$$r_4 + r_1 > r_2 + r_3 \cap r_4 + r_2 < r_1 + r_3 \cap r_4 + r_3 > r_1 + r_2 \quad (10.31)$$

$$r_4 + r_1 < r_2 + r_3 \cap r_4 + r_2 < r_1 + r_3 \cap r_4 + r_3 < r_1 + r_2 \quad (10.32)$$

Table 10.3 shows the eleven types of 3-DOF PPMs, where 3-crank $T-i$ ($i = 1, 2, 3$, and 4) means the 3-crank-type- i 3-DOF PPMs; 3-rocker $T-i$ ($i = 1, 2, 3$, and 4) expresses the 3-rocker-type- i 3-DOF PPMs; and Change point $T-i$ ($i = 1, 2$, and 3) denotes the change-point-type- i 3-DOF PPMs. Therefore, there are four types of 3-crank 3-DOF PPMs, four types of 3-rocker 3-DOF PPMs and three types of change point 3-DOF PPMs (as shown in Table 10.3).

Model of Solution Space for 3-DOF Delta Parallel Robots

Delta parallel robots (DPR) are a specific class of parallel manipulators that can position a platform in a region of 3-D space so that the platform remains parallel to a specified reference plane. DPRs have applications in the manipulation of lightweight objects for the electronic, food, and pharmaceutical industries. Although researchers have investigated the forward and inverse kinematics, inverse dynamics, sizes, singularities, and working volume of DPRs [44–50], insufficient attention has been given to the analysis of relationships involving the link lengths of DPRs.

We shall consider a DPR, as shown in Fig. 10.9, where R_i is the length of the i th link; R_1, R_5, R_9 , are the lengths of the input links; R_2, R_6, R_{10} are the lengths of the parallelogram supporting rods; R_3, R_7, R_{11} are the lengths of the output links; and R_4, R_8, R_{12} are the lengths of the fixed link.

TABLE 10.3 Complete Classification of 3-DOF PPMs

No.	Region	Proposed Name	Characteristics of link lengths	Dimensional Characteristics
1	I	3-crank T-1	r_1 =the shortest	Inequality (10.25)
2	II	3-crank T-2	r_2 =the shortest	Inequality (10.26)
3	III	3-crank T-3	r_3 =the shortest	Inequality (10.27)
4	IV	3-rocker T-4	r_3 =the longest	Inequality (10.28)
5	V	3-rocker T-1	r_2 =the longest	Inequality (10.29)
6	VI	3-rocker T-2	r_1 =the longest	Inequality (10.30)
7	VII	3-rocker T-3	r_4 =the longest	Inequality (10.31)
8	VIII	3-crank T-4	r_4 =the shortest	Inequality (10.32)
9	Line 1	Change point T-1	$r_1 + r_4 = r_2 + r_3$	Equality (10.22)
10	Line 2	Change point T-2	$r_2 + r_4 = r_1 + r_3$	Equality (10.23)
11	Line 3	Change point T-3	$r_3 = r_4 + r_1 + r_2$	Equality (10.24)

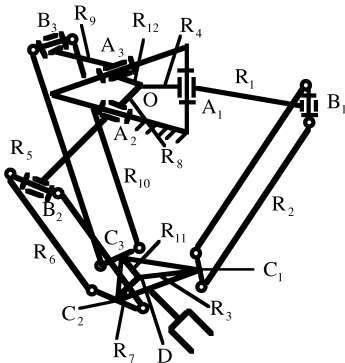


FIGURE 10.9 A typical 3-DOF DPR.

Nondimensional Parameters of DPRs

We define

$$L = \frac{1}{12} \sum_{i=1}^{12} R_i \quad (10.33)$$

By dividing the link length R_i ($i = 1, 2, \dots, 12$) by L , we obtain twelve nondimensional parameters

$$r_i = R_i / L \quad (i = 1, 2, \dots, 12) \quad (10.34)$$

Therefore,

$$\sum_{i=1}^{12} r_i = 12 \quad (10.35)$$

Gosselin [31] proposed that parallel robotic manipulators should be symmetric because the tasks to be performed by the manipulators are unknown and unpredictable. By symmetry, one obtains

$$\begin{array}{ll} R_1 = R_5 = R_9 & r_1 = r_5 = r_9 \\ R_2 = R_6 = R_{10} & r_2 = r_6 = r_{10} \\ R_3 = R_7 = R_{11} & r_3 = r_7 = r_{11} \\ R_4 = R_8 = R_{12} & r_4 = r_8 = r_{12} \end{array} \quad \text{and} \quad (10.36)$$

The symmetry assumption will be used throughout this paper. From Eqs. (10.35) and (10.36), the relative link lengths of the DPR satisfy the relationship

$$r_1 + r_2 + r_3 + r_4 = 4 \quad (10.37)$$

It is well known that a DPR cannot be synthesized if one of the link lengths exceeds the following maximum values:

$$r_1 = 4, \quad r_2 = 4, \quad r_3 = 2, \quad \text{and} \quad r_4 = 2 \quad (10.38)$$

If one of all the link lengths r_i ($i = 1, 2, 3$, and 4) satisfies Eqs. (10.37) and (10.38), the DPR can be synthesized, but it cannot move. Eq. (10.38) is the zero-mobility condition for DPRs, which defines four zero-mobility planes.

Model of Solution Space for DPRs

Let r_1 , r_2 , and r_3 be orthogonal coordinate axes. Using Eqs. (10.37) and (10.38) and the conditions

$$0 < r_1 < 4, \quad 0 < r_2 < 4, \quad 0 \leq r_3 < 2, \quad \text{and} \quad 0 \leq r_4 < 2, \quad (10.39)$$

we can establish the model of the solution space as shown in Fig. 10.10. The model is an irregular hexahedron ABCDEFG as shown in Fig. 10.10(b), for which any possible combination of the link lengths is represented by values of the links r_1 , r_2 , r_3 , and r_4 . The resulting model provides a means to reduce the 12-D infinite space to the 3-D finite one.

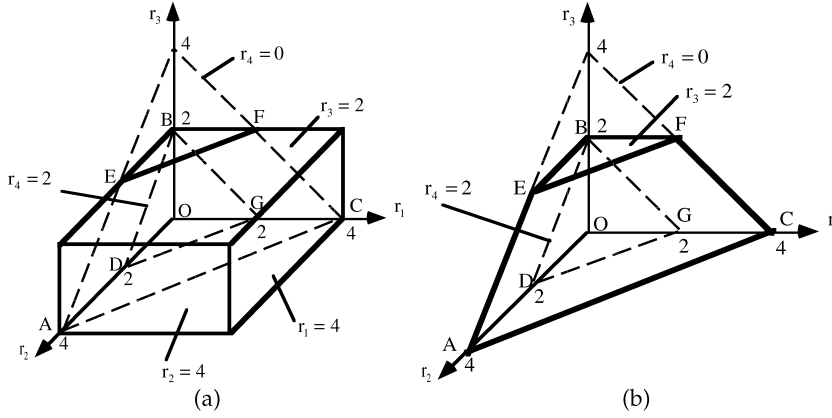


FIGURE 10.10 The model of the solution space for 3-DOF DPRs. (a) $r_1 + r_4 = r_2 + r_3$, (b) $r_2 + r_4 = r_1 + r_3$.

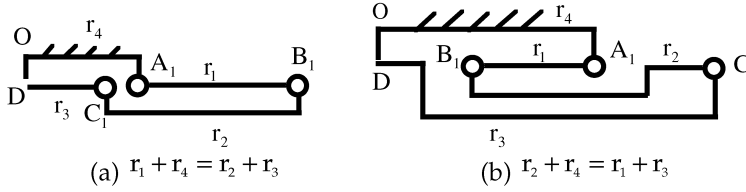


FIGURE 10.11 Two types of the branches of change point DPR. (a) $r_4 = 0$, (b) $0 < r_4 < 1$, (c) $r_4 = 1$, (d) $1 < r_4 < 2$, (e) $r_4 = 2$.

Planar Closed Configurations

Consider the link r_i ($i = 1, 2, 3$, and 4) in a DPR, where the sum of any two link lengths, except r_3 and r_4 , is equal to the sum of the other two link lengths. For this situation we call the DPR a change point one. Physically, this means that all four links may be collinear (as shown in Fig. 10.11). Therefore, two change point planes are defined by:

$$r_1 + r_4 = r_2 + r_3 \quad (10.40)$$

$$r_2 + r_4 = r_1 + r_3. \quad (10.41)$$

By giving several values for r_4 , a set of plane equations can be obtained from Eq. (10.37). Therefore, r_4 is an auxiliary coordinate axis in the model of the solution space. When r_4 is given, Eq. (10.37) can be expressed as

$$r_1 + r_2 + r_3 = 4 - r_4 \quad (10.42)$$

which is an equation of a plane. When $r_4 = 0$; $r_4 < 1$; $r_4 = 1$; $r_4 > 1$; and $r_4 = 2$, respectively, a set of planes is obtained. These planes are called “planar closed configurations” with coordinates r_1, r_2, r_3 , which are isosceles trapezoids, as shown in Fig. 10.12.

Using Eqs. (10.40) and (10.41), lines 1 and 2 can be drawn on the five types of planar closed configurations as shown in Fig. 10.12. These two lines are change point lines on which all the change point DPRs exist.

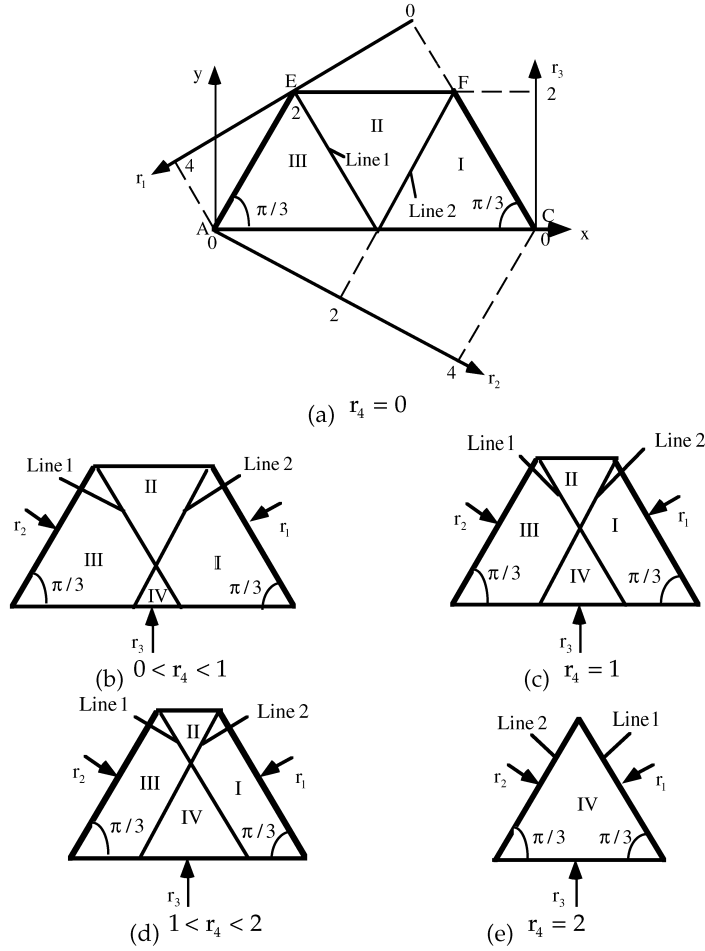


FIGURE 10.12 Five types of planar closed configurations.

Coordinate Transformation

As shown in Fig. 10.12(a), the planar closed configurations have coordinates r_1 r_2 r_3 . Only two of these are independent. For convenience, we should utilize two orthogonal coordinates x y to express r_1 r_2 r_3 . Thus, by use of

$$\begin{pmatrix} x \\ y \end{pmatrix} = \begin{bmatrix} 2\sqrt{3}/3 & \sqrt{3}/3 \\ 0 & 1 \end{bmatrix} \begin{pmatrix} r_2 \\ r_3 \end{pmatrix}, \quad (10.43)$$

we can transform coordinates r_1 r_2 r_3 into x y . Eq. (10.43) is very useful for construction of the performance atlases. In addition, if the values of x and y are known, the values of r_1 , r_2 , and r_3 can be calculated by

$$\begin{pmatrix} r_1 \\ r_2 \\ r_3 \end{pmatrix} = \begin{bmatrix} -\sqrt{3}/2 & -1/2 & 4 - r_4 \\ \sqrt{3}/2 & -1/2 & 0 \\ 0 & 1 & 0 \end{bmatrix} \begin{pmatrix} x \\ y \\ 1 \end{pmatrix} \quad (10.44)$$

Classification of DPRs

By using Eqs. (10.40) and (10.41), lines 1 and 2 can be drawn on the planar closed configurations (as shown in Fig. 10.12). These lines separate planar closed configurations into four regions I, II, III, and IV. Each expresses a class of DPRs. For convenience of classification, we define a virtual planar slider-crank mechanism $OA_1B_1C_1D$, which is a branch of the Delta mechanism as shown in Fig. 10.13.

Because Delta mechanisms treated in this section are symmetric, we only need to consider the four links r_i ($i = 1, 2, 3$, and 4) which describe a virtual planar slider-crank mechanism. In Fig. 10.13, point D is the center of the platform when the three input links have the same angle with respect to their start positions, i.e., when the three input links r_1 , r_5 and r_9 are located at the same plane with the frame. We assume point D is a virtual slider that can slide only along the line OD , because only when the center of the platform (point D) moves along the line OD do the three input links have the same motion and it is possible to investigate the mobility of Delta mechanisms. From the virtual planar slider-crank mechanism, we derive the velocity equation

$$\dot{\phi}_1 = J\dot{\phi}_2$$

We know that when input link r_1 is located at the extreme position and the angular velocity $\dot{\phi}_2$ is non-zero, the angular velocity $\dot{\phi}_1$ must be zero. Thus, we obtain the results:

$$\dot{\phi}_1 = 0 \quad \text{and} \quad J = 0$$

From this, we derive the conditions which can be used to determine the extreme positions of link r_1 , as shown in Fig. 10.14, that is,

$$\phi_2 = \frac{\pi}{2} \quad \text{or} \quad -\frac{\pi}{2}$$

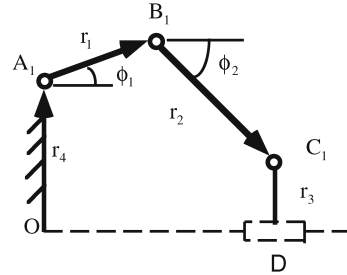


FIGURE 10.13 Virtual planar slider-crank mechanism for DPRs. (a) $\phi_2 = -\frac{\pi}{2}$, (b) $\phi_2 = \frac{\pi}{2}$.

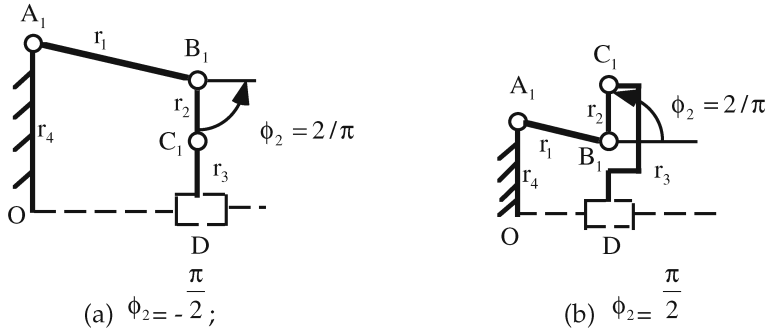


FIGURE 10.14 Virtual mechanisms with extreme positions of input link r_1 . (a) Perspective view, (b) top view.

or these equations.

$$\phi_{1 \max} = \sin^{-1}[(r_2 + r_3 - r_4)/r_1] \quad (10.45)$$

$$\phi_{1 \min} = \sin^{-1}[(r_3 - r_2 - r_4)/r_1] \quad (10.46)$$

That is, if the virtual slider-crank mechanism satisfies one of the Eqs. (10.45) and (10.46), the revolving input link does not exist. On the contrary, if it does not satisfy both of them at the same time, the conditions for existence of the revolving input link r_1 are obtained:

$$|(r_2 + r_3 - r_4)/r_1| \geq 1 \quad (10.47)$$

$$|(r_3 - r_2 - r_4)/r_1| \geq 1 \quad (10.48)$$

From Eqs. (10.47) and (10.48), we can further derive the conditions for existence of the revolving input link of the virtual slider-crank mechanism as

$$r_1 + r_4 \leq r_2 + r_3 \quad (10.49)$$

$$r_1 + r_3 \leq r_2 + r_4 \quad (10.50)$$

Using these conditions, we can classify the Delta mechanisms. [Table 10.4](#) describes the resulting classification. We achieve six classes of Delta parallel robots, that is, one type of 3-crank Delta mechanisms, three types of 3-rocker Delta mechanisms, and two types of change point Delta mechanisms. [Table 10.4](#) also shows the dimensional characteristics of these classes.

Model of Solution Space for F/T Sensors Based on Stewart Platform

Force/torque (F/T) sensors can be used for monitoring forces of variable directions and intensity (such as wind-tunnel testing, adaptive control of machines and thrust stand testing of rocket engines [51]), measuring inertia force (computer input device: Smartpen [52]) or contact force to feed it back to the command signal and estimating the location of the contacts between robot and environment through force measurements so that they have been applied to manufacturing, robotics, military, electronic, and computer industries, and so on. Therefore, a multiaxis F/T sensor is a critical component of an automated system for extending the capability of manipulation and assembly, especially with contact tasks that require mechanical operations involving interaction with the environment or objects.

Although many kinds of F/T sensors have been developed, Stewart-platform transducer F/T sensor is a novel and specific one. Some research has been devoted to this kind of sensor. Kerr [53] presented Stewart-platform transducer force sensor, and Nguyen [54] and Ferraresi [55] analyzed Stewart-platform

TABLE 10.4 Classification of DPRs

No.	Region	Name	Dimensional Characteristics
1	I	3-Crank DPR	$r_1 + r_4 < r_2 + r_3 \cap r_1 + r_3 < r_2 + r_4$
2	II	3-Rocker 1 DPR	$r_1 + r_4 < r_2 + r_3 \cap r_1 + r_3 > r_2 + r_4$
3	III	3-Rocker 2 DPR	$r_1 + r_4 > r_2 + r_3 \cap r_1 + r_3 > r_2 + r_4$
4	IV	3-Rocker 3 DPR	$r_1 + r_4 > r_2 + r_3 \cap r_1 + r_3 < r_2 + r_4$
5	line 1	Change Point 1DPR	$r_1 + r_4 = r_2 + r_3$
6	line 2	Change Point 2DPR	$r_1 + r_3 = r_2 + r_4$

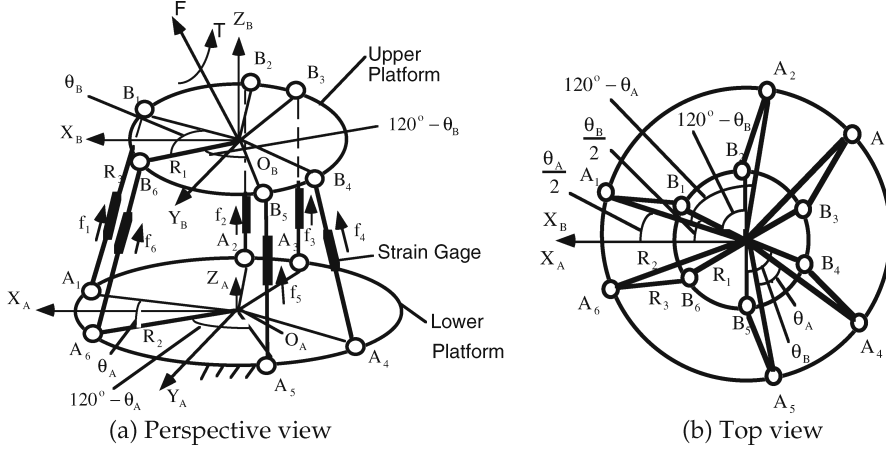


FIGURE 10.15 The mechanism of the sensor based on Stewart platform.

force sensor. Because the structure of Stewart-platform force sensor is a kind of parallel mechanism, the technique for analysis and design of parallel mechanisms can be used for the F/T sensor.

In this section we propose a model of the solution space for the structures of the F/T sensors based on the Stewart platform, which is the foundation for investigation of the design method of the sensor.

Consider the F/T sensor mechanism based on Stewart platform as shown in Fig. 10.15. Because the link lengths may have a wide range of possible values, it is convenient to avoid explicit use of the physical sizes of the mechanisms during analysis and design. We shall define normalized parameters of the sensor mechanisms and construct the model of the solution space.

Since the parallel mechanisms should be symmetric [31], there are four parameters in the sensor mechanism as shown in Fig. 10.15, that is, R_1 , R_2 , R_3 , and θ_{AB} , where

$$\begin{aligned}\theta_{AB} &= |\theta_A - \theta_B| \quad (0^\circ < \theta_{AB} < 120^\circ) \\ \theta_A &= \angle A_2 A_3 = \angle A_4 A_5 = \angle A_6 A_1 \\ \theta_B &= \angle B_2 B_3 = \angle B_4 B_5 = \angle B_6 B_1 \\ 180^\circ - \theta_A &= \angle A_1 A_2 = \angle A_3 A_4 = \angle A_5 A_6 \\ 180^\circ - \theta_B &= \angle B_1 B_2 = \angle B_3 B_4 = \angle B_5 B_6\end{aligned}$$

Let

$$L = (R_1 + R_2 + R_3)/3 \quad (10.51)$$

$$r_1 = R_1/L, \quad r_2 = R_2/L, \quad \text{and} \quad r_3 = R_3/L \quad (10.52)$$

where R_i is the length of link i , r_i is the normalized, nondimensional length of link i , and L is the average link length of the mechanism. Therefore, the sum of the normalized link lengths is

$$r_1 + r_2 + r_3 = 3 \quad (10.53)$$

If the mechanism can be assembled, the normalized link lengths satisfy

$$0 < r_1 < 1.5, \quad 0 < r_2 < 1.5, \quad \mu < r_3 < 3 \quad (10.54)$$

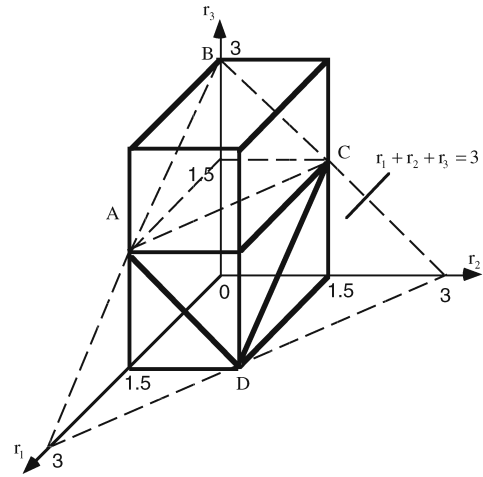


FIGURE 10.16 A physical model of the solution space for the sensor mechanisms.

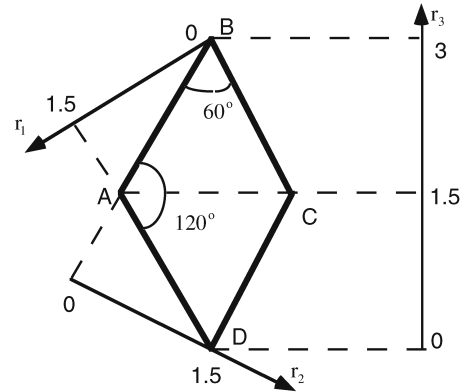


FIGURE 10.17 Planar closed configuration of the solution space.

where

$$\mu = \sqrt{r_1^2 + r_2^2 - 2r_1r_2\cos\left(\frac{\theta_{AB}}{2}\right)} \quad \text{and} \quad 0 < \mu \quad (10.55)$$

From the conditions (10.53) and (10.54), a physical model of the solution space for the sensor mechanisms can be constructed as shown in Fig. 10.16, which is the rhombus ABCD. By placing the model on a plane, the planar closed configuration of the solution space with three coordinates can be obtained as shown in Fig. 10.17. Within the model ABCD, we can investigate relationships between the criteria and parameters of the sensor mechanisms.

10.3 Performance Evaluation Criteria for Design of Robotic Mechanisms

The design of robotic mechanisms can be simplified by the criteria that permit the analysis of tradeoffs. In recent years, researchers have presented some performance criteria based on workspace geometry [56–64], isotropy [65–68], dexterity [69–73], global conditioning index [43], and singularity [74–76]. By use of the criteria, optimization has been used as a design tool [31, 77–81].

In this section, we list the major performance criteria that provide a foundation for using the technique of the solution space models to design robotic mechanisms.

Three Kinds of Workspaces

We consider a robot consisting of a manipulator and an end-effector. The robot structure may be serial or parallel. The workspace of a robot defines the useful positions and orientations of the end-effector. In this section, we consider the following three types of workspaces:

- Reachable Workspace: the set of points attainable by a point attached to the end-effector.
- Dextrous Workspace: the set of points of the workspace in which an end-effector can have arbitrary orientations.
- Global Workspace: the set of points that the end-effector can reach when all orientations of the end-effector are given [31].

Three Kinds of Singularities

To improve robot performance, singular configurations must be identified at the design stage because singularities lead to an instantaneous change in the degrees of freedom of the mechanism. They also result in a loss of the controllability and degradation of the natural stiffness that may lead to high joint forces or torques. There are three kinds of singularities [75]. The first type occurs when

$$\det(J) = 0 \quad (10.56)$$

where $[J]$ is the Jacobian matrix of the robotic mechanism. The corresponding configurations are located at the boundary of the workspace of the manipulator or on internal boundaries between regions of the workspace in which the number of solutions of the inverse kinematic problem differs.

A second type of singularity occurs when

$$\det(J) \rightarrow \infty. \quad (10.57)$$

This type of singularity results in an unwanted degree of freedom of the manipulator. Such a configuration must be avoided because the manipulator is not controllable. This type of singularity, however, cannot occur in serial manipulators.

A third type of singularity only occurs for parallel manipulators,

$$\det(J) \rightarrow \frac{0}{0}. \quad (10.58)$$

Global Conditioning Index

The global conditioning index is an important measure for control of the manipulator. It is defined as the inverse of the condition number of the Jacobian matrix $[J]$ integrated over the reachable workspace and divided by the volume of the workspace. In particular, a large value of the index ensures that the manipulator can be precisely controlled. To evaluate the global behavior of a manipulator, Gosselin [43] defined the global conditioning index,

$$\eta = A/B, \quad (10.59)$$

where

$$\begin{aligned} A &= \int_w \left(\frac{1}{\|J\| \|J^{-1}\|} \right) dw \\ B &= \int_w dw \end{aligned} \quad (10.60)$$

Here, B is the volume of the reachable workspace w , and

$$\|J\| = \sqrt{\text{tr}\left(J^{\frac{1}{n}}[I]J^T\right)} \quad (10.61)$$

where n is the dimension of the square matrix $[J]$, and $[I]$ is the identity matrix having the same dimension as $[J]$.

Global Velocity Index

The global velocity index is a measure of robotic speed. We define the global maximum and minimum velocity indices to be the extreme values of the end-effector velocities integrated over the reachable workspace and divided by the volume of the workspace.

The linear velocity V and angular velocity ω of the end-effector are related to the input velocities $\dot{\phi}$ by

$$\begin{pmatrix} V \\ \omega \end{pmatrix} = [J](\dot{\phi}) = \begin{bmatrix} J_v \\ J_\omega \end{bmatrix}(\dot{\phi}) \quad (10.62)$$

From Eq. (62), we obtain

$$\|V\|^2 = (\dot{\phi})^T [J_v]^T [J_v](\dot{\phi}) \quad (10.63)$$

$$\|\omega\|^2 = (\dot{\phi})^T [J_\omega]^T [J_\omega](\dot{\phi}) \quad (10.64)$$

Let

$$\|\dot{\phi}\|^2 = (\dot{\phi})^T (\dot{\phi}) = 1, \quad (10.65)$$

$$L_v = (\dot{\phi})^T [J_v]^T [J_v](\dot{\phi}) - \lambda_v [(\dot{\phi})^T (\dot{\phi}) - 1] \quad (10.66)$$

and

$$L_\omega = (\dot{\phi})^T [J_\omega]^T [J_\omega](\dot{\phi}) - \lambda_\omega [(\dot{\phi})^T (\dot{\phi}) - 1] \quad (10.67)$$

where λ_v and λ_ω are Lagrange multipliers. From Eqs. (10.66) and (10.67), necessary conditions for extreme values of the linear and angular velocities of the end-effector are

$$\frac{\partial L_v}{\partial \lambda_v} = 0 : (\dot{\phi})^T (\dot{\phi}) - 1 = 0, \quad \frac{\partial L_v}{\partial (\dot{\phi})} = 0 : [J_v]^T [J_v](\dot{\phi}) - \lambda_v (\dot{\phi}) = 0 \quad (10.68)$$

$$\frac{\partial L_\omega}{\partial \lambda_\omega} = 0 : (\dot{\phi})^T (\dot{\phi}) - 1 = 0, \quad \frac{\partial L_\omega}{\partial (\dot{\phi})} = 0 : [J_\omega]^T [J_\omega](\dot{\phi}) - \lambda_\omega (\dot{\phi}) = 0 \quad (10.69)$$

From Eqs. (10.68) and (10.69), we see that λ_v and λ_ω are eigenvalues of $[J_v]^T [J_v]$ and $[J_\omega]^T [J_\omega]$, respectively, so that extreme values of the velocities are

$$\|V_{\max}\| = \sqrt{\lambda_{v \max}} \quad \text{and} \quad \|V_{\min}\| = \sqrt{\lambda_{v \min}} \quad (10.70)$$

$$\|\omega_{\max}\| = \sqrt{\lambda_{\omega \max}} \quad \text{and} \quad \|\omega_{\min}\| = \sqrt{\lambda_{\omega \min}} \quad (10.71)$$

Because $[J]$ depends on the configuration of the manipulator, extreme values of the end-effector velocity cannot characterize the robotic performance. We define global velocity index, a criterion involving the end-effector velocity, as follows:

$$\gamma_{V \max} = \frac{C_{V \max}}{B} \quad \text{and} \quad \gamma_{V \min} = \frac{C_{V \min}}{B} \quad (10.72)$$

$$\gamma_{\omega \max} = \frac{C_{\omega \max}}{B} \quad \text{and} \quad \gamma_{\omega \min} = \frac{C_{\omega \min}}{B} \quad (10.73)$$

where $\gamma_{V \max}$ and $\gamma_{V \min}$ are the global maximum and minimum linear velocity indices, respectively; $\gamma_{\omega \max}$ and $\gamma_{\omega \min}$ are the global maximum and minimum angular velocity indices, respectively; B is the volume of the reachable workspace; and

$$C_{V \max} = \int_w (V_{\max}) dw \quad \text{and} \quad C_{V \min} = \int_w (V_{\min}) dw,$$

$$C_{\omega \max} = \int_w (\omega_{\max}) dw \quad \text{and} \quad C_{\omega \min} = \int_w (\omega_{\min}) dw.$$

Global Payload Index

The global payload index is a measure of the capability of payload that can be handled by the robotic mechanisms. We define the global maximum and minimum payload indices to be the extreme values of the robotic payload integrated over the reachable workspace of the robot and divided by the volume of the workspace.

The external force F and torque T applied at the end-effector are related to the input force or torque τ by

$$(\tau) = [J]^T \begin{pmatrix} F \\ T \end{pmatrix} \quad (10.74)$$

If $\det(J^T) \neq 0$, we obtain

$$\begin{pmatrix} F \\ T \end{pmatrix} = [J^T]^{-1}(\tau) = \begin{bmatrix} J_F \\ J_T \end{bmatrix}(\tau) \quad (10.75)$$

Using the same method as in the previous section,

$$\|F_{\max}\| = \sqrt{\lambda_{F \max}} \quad \text{and} \quad \|F_{\min}\| = \sqrt{\lambda_{F \min}} \quad (10.76)$$

$$\|T_{\max}\| = \sqrt{\lambda_{T \max}} \quad \text{and} \quad \|T_{\min}\| = \sqrt{\lambda_{T \min}} \quad (10.77)$$

where $\lambda_{F \max}$ and $\lambda_{F \min}$ are the maximum and minimum eigenvalues of the matrix $[J_F]^T [J_F]$, respectively; and $\lambda_{T \max}$ and $\lambda_{T \min}$ are the maximum and minimum eigenvalues of the matrix $[J_T]^T [J_T]$, respectively.

When the input torque is a unit vector, the global payload indices are

$$\gamma_{F \max} = \frac{C_{F \max}}{B} \quad \text{and} \quad \gamma_{F \min} = \frac{C_{F \min}}{B} \quad (10.78)$$

$$\gamma_{T \max} = \frac{C_{T \max}}{B} \quad \text{and} \quad \gamma_{T \min} = \frac{C_{T \min}}{B} \quad (10.79)$$

where $\gamma_{F \max}$ and $\gamma_{F \min}$ are the global maximum and minimum force payload indices, respectively; $\gamma_{T \max}$ and $\gamma_{T \min}$ are the global maximum and minimum torque payload indices, respectively; and

$$C_{F \max} = \int_w \|F_{\max}\| dw \quad \text{and} \quad C_{F \min} = \int_w \|F_{\min}\| dw \quad (10.80)$$

$$C_{T \max} = \int_w \|T_{\max}\| dw \quad \text{and} \quad C_{T \min} = \int_w \|T_{\min}\| dw \quad (10.81)$$

Global Deformation Index

The global deformation index is a measure of the stiffness of the robotic end-effector. We define the global maximum and minimum deformation indices to be the extreme values of the end-effector deformation integrated over the reachable workspace of the robot and divided by the volume of the workspace.

The input forces or torques are related to the deformation by

$$(\tau) = [K](\Delta q) \quad (10.82)$$

where

$$\begin{aligned} [K] &= [I](k_1 \quad k_2 \dots k_m)^T \\ (\Delta q) &= (\Delta q_1 \quad \Delta q_2 \dots \Delta q_m)^T \end{aligned} \quad (10.83)$$

In Eq. (10.83), Δq_i is the deformation of joint i of the input link i ; k_i is the stiffness of actuator i at joint i ($i = 1, 2, \dots, m$); and $[I]$ is an $m \times m$ identity matrix. We assume

$$k_i = k, \quad (10.84)$$

which means that all actuators have the same stiffness. From Eqs. (10.74) and (10.82), the deformation (D) of the end-effector is

$$(D) = [J](\Delta q) = [J][K]^{-1}[J]^T(F \ T)^T = [C](F \ T)^T \quad (10.85)$$

From Eqs. (10.84) and (10.85), we obtain a representation for the compliance matrix of the manipulator as

$$[C] = [J][K]^{-1}[J]^T = \frac{1}{k}[J][J]^T \quad (10.86)$$

$[C]^{-1}$ is the stiffness matrix. Because we only investigate the relationship between the criteria and link lengths of robots, let k be equal to 1. From Eqs. (10.85) and (10.86), we obtain

$$(D) = \begin{pmatrix} D_p \\ D_o \end{pmatrix} = [C] \begin{pmatrix} F \\ T \end{pmatrix} = \begin{bmatrix} C_p \\ C_o \end{bmatrix} \begin{pmatrix} F \\ T \end{pmatrix} \quad (10.87)$$

where (D_p) and (D_o) express the position deformation and orientation deformation of the end-effector, respectively. Thus, we have

$$(D_p) = [C_p](F \ T)^T \quad (10.88)$$

$$(D_o) = [C_o](F \ T)^T \quad (10.89)$$

Using the method of Section 3.4, we derive

$$\|D_{p\max}\| = \sqrt{\lambda_{D_p\max}} \quad \text{and} \quad \|D_{p\min}\| = \sqrt{\lambda_{D_p\min}} \quad (10.90)$$

$$\|D_{o\max}\| = \sqrt{\lambda_{D_o\max}} \quad \text{and} \quad \|D_{o\min}\| = \sqrt{\lambda_{D_o\min}} \quad (10.91)$$

where $\lambda_{D_p\max}$ and $\lambda_{D_p\min}$ are maximum and minimum eigenvalues of $[C_p]^T[C_p]$, respectively, and $\lambda_{D_o\max}$ and $\lambda_{D_o\min}$ are maximum and minimum eigenvalues of $[C_o]^T[C_o]$.

The global positional and orientational deformation indices can be represented by

$$\gamma_{D_p\max} = \frac{A_{p\max}}{B} \quad \text{and} \quad \gamma_{D_p\min} = \frac{A_{p\min}}{B} \quad (10.92)$$

$$\gamma_{D_o\max} = \frac{A_{o\max}}{B} \quad \text{and} \quad \gamma_{D_o\min} = \frac{A_{o\min}}{B} \quad (10.93)$$

where $\gamma_{D_p\max}$ and $\gamma_{D_p\min}$ are the global maximum and minimum position deformation indices, respectively; $\gamma_{D_o\max}$ and $\gamma_{D_o\min}$ are the global maximum and minimum orientation deformation indices, respectively; and

$$A_{p\max} = \int_w \|D_{p\max}\| dw \quad \text{and} \quad A_{p\min} = \int_w \|D_{p\min}\| dw ,$$

$$A_{o\max} = \int_w \|D_{o\max}\| dw \quad \text{and} \quad A_{o\min} = \int_w \|D_{o\min}\| dw .$$

Global Error Index

The global error index is a measure of accuracy of the robotic end-effector. We define the global maximum and minimum error indices to be the extreme values of the end-effector error integrated over the reachable workspace of the robot and divided by the volume of the workspace.

Errors in the end-effector motion can be divided into two parts,

$$(\Delta E) = (\Delta E_\theta) + (\Delta E_D) \quad (10.94)$$

where (ΔE_θ) is the error concerning the input motion tolerance $\Delta\theta$; and (ΔE_D) is the error relative to the tolerance of the dimensions of the robotic mechanism. Therefore, we obtain the position error of the end-effector as

$$(\Delta E_p) = (\Delta E_{\theta p}) + (\Delta E_{Dp}) \quad (10.95)$$

and the orientation error of the end-effector as

$$(\Delta E_O) = (\Delta E_{\theta O}) + (\Delta E_{DO}). \quad (10.96)$$

Since

$$\begin{pmatrix} \Delta E_{\theta P} \\ \Delta E_{\theta O} \end{pmatrix} = [J](\Delta \theta) = \begin{bmatrix} J_V \\ J_\omega \end{bmatrix}(\Delta \theta) \quad (10.97)$$

Comparing Eq. (10.97) and (10.62), we obtain

$$\gamma_{E_{\theta P} \max} = \gamma_{V \max} \quad \text{and} \quad \gamma_{E_{\theta P} \min} = \gamma_{V \min} \quad (10.98)$$

$$\gamma_{E_{\theta O} \max} = \gamma_{\omega \max} \quad \text{and} \quad \gamma_{E_{\theta O} \min} = \gamma_{\omega \min} \quad (10.99)$$

where $\gamma_{E_{DP} \max}$ and $\gamma_{E_{DP} \min}$ are the global maximum and minimum position error indices with respect to the input motion tolerance $\Delta \theta$, respectively; $\gamma_{E_{\theta O} \max}$ and $\gamma_{E_{\theta O} \min}$ are the global maximum and minimum orientation error indices with respect to the input motion tolerance $\Delta \theta$, respectively.

Next, relative to the dimensional tolerance of the mechanism, we consider errors

$$\begin{pmatrix} \Delta E_{DP} \\ \Delta E_{DO} \end{pmatrix} = [J_D](\Delta D) = \begin{bmatrix} J_{DP} \\ J_{DO} \end{bmatrix}(\Delta D) \quad (10.100)$$

where (ΔD) is the dimensional tolerance of the robotic mechanism, and $[J_D]$ is the error transformation matrix with respect to the dimensional error.

Using the method in the section entitled ‘‘Global Velocity Index,’’ we derive

$$\|\Delta E_{DP \max}\| = \sqrt{\lambda_{E_{DP} \max}} \quad \text{and} \quad \|\Delta E_{DP \min}\| = \sqrt{\lambda_{E_{DP} \min}} \quad (10.101)$$

$$\|\Delta E_{DO \max}\| = \sqrt{\lambda_{E_{DO} \max}} \quad \text{and} \quad \|\Delta E_{DO \min}\| = \sqrt{\lambda_{E_{DO} \min}} \quad (10.102)$$

where $\lambda_{E_{DP} \max}$ and $\lambda_{E_{DP} \min}$ are maximum and minimum eigenvalues of matrix $[J_{DP}]^T [J_{DP}]$, respectively; $\lambda_{E_{DO} \max}$ and $\lambda_{E_{DO} \min}$ are maximum and minimum eigenvalues of $[J_{DO}]^T [J_{DO}]$. Therefore, the global position and orientation error indices relative to the dimensional tolerances can be obtained by

$$\gamma_{E_{DP} \max} = \frac{A_{E_{DP} \max}}{B} \quad \text{and} \quad \gamma_{E_{DP} \min} = \frac{A_{E_{DP} \min}}{B} \quad (10.103)$$

$$\gamma_{E_{DO} \max} = \frac{A_{E_{DO} \max}}{B} \quad \text{and} \quad \gamma_{E_{DO} \min} = \frac{A_{E_{DO} \min}}{B} \quad (10.104)$$

where $\gamma_{E_{DP} \max}$ and $\gamma_{E_{DP} \min}$ are the global maximum and minimum position error indices relative to the tolerance of the dimensions of the mechanism, respectively; $\gamma_{E_{DO} \max}$ and $\gamma_{E_{DO} \min}$ are the global maximum and minimum orientation error indices relative to the dimensional tolerance of the mechanism, respectively; and

$$A_{E_{DP} \max} = \int_w \|\Delta E_{DP \max}\| dw \quad \text{and} \quad A_{E_{DP} \min} = \int_w \|\Delta E_{DP \min}\| dw,$$

$$A_{E_{DO} \max} = \int_w \|\Delta E_{DO \max}\| dw \quad \text{and} \quad A_{E_{DO} \min} = \int_w \|\Delta E_{DO \min}\| dw,$$

The criteria described in this section involve kinematic and dynamic properties and characterize robot performance. These results provide a basis for analyzing and designing robotic mechanisms. Because the solution space model applies to both serial and parallel robotic mechanisms, the criteria have wide application to many different types of robotic mechanisms.

10.4 Performance Atlases for Design of Serial Robots with Three Moving Links

Human arms, legs, fingers, and limbs of animals and insects can be viewed as mechanisms with three moving links. Fingers of dextrous hands, arms of industrial robots, and legs of walking machines often consist of three moving links. Therefore, an understanding of the relationships between the criteria and the dimensions of three-moving-link mechanisms is of great importance for design of fingers, arms, and legs of robotics machines.

In this section, we use the technique of physical models of solution space proposed in Section 10.2 and the evaluation criteria presented in Section 10.3 to investigate the relationships between the criteria and the dimensions of mechanisms with three moving links. In addition, the distribution of the 63 commercially available industrial and research robots within the model of solution space is discussed.

Robotic Principle Motion

Although a biological system can provide compact actuation of fingers, arms, and legs with multiple degrees of freedom, planar motion provides the most significant contribution to kinematic and dynamic performance. We define the principle motions produced by robotic mechanisms with three moving links as that produced by joints sharing a common and parallel axis. Since industrial robots often are built in this manner, this type of motion is very important for design.

By using the theory of the principle motions, many robotic mechanisms with three moving links as shown in Fig. 10.3 can be simplified as 3-DOF planar mechanisms. For this reason, the treatment described in this chapter is restricted to mechanisms that produce principle motions, that is, 3-DOF planar serial mechanisms as shown in Fig. 10.18.

Atlases of Workspace Criteria

The workspace of a manipulator determines attainable positions and orientations of its end-effector. We shall consider the reachable workspace, dextrous workspace, and global workspace. The atlases of reachable, dextrous, and global workspaces can be represented on the solution space as shown in Figs. 10.19, 10.21, and 10.22.

Reachable Workspace Atlas

The reachable workspace of a 3-DOF planar serial mechanism, as shown in Fig. 10.18, consists of all points traversed by the end effector. Two types of reachable workspaces are the loop and the plate as

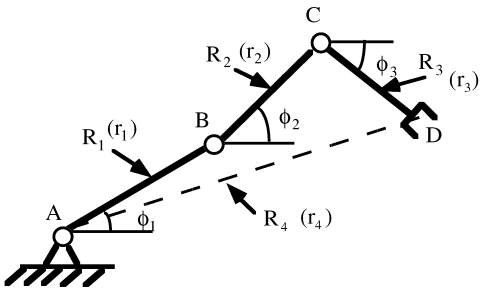
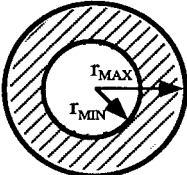

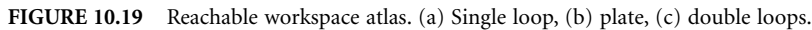


FIGURE 10.18 A 3-DOF planar mechanism.

Region	Shape	r_{MAX}	r_{MIN}	Area
I		$r_1 + r_2 + r_3$	$r_2 - r_1 - r_3$	$4\pi(3 - r_1)r_1$
II		$r_1 + r_2 + r_3$	$r_2 - r_1 - r_3$	$4\pi(3 - r_2)r_2$
III		$r_1 + r_2 + r_3$	$r_3 - r_1 - r_2$	$4\pi(3 - r_3)r_3$
IV		$r_1 + r_2 + r_3$	0	9π



- In region IV, the reachable workspace has maximum area equal to 9π .
- In regions I, II, and III, the area of the reachable workspace is inversely proportional to $r_p, p = 1, 2, 3$, respectively.
- The reachable workspace is symmetric about axes $r_1 = r_2$, $r_1 = r_3$, and $r_2 = r_3$, respectively.

The dextrous workspace of a robot is an important criterion for performance evaluation. Since the robot end-effector may have to achieve a given pose from a particular direction, it is of practical interest to determine these directions.

For the convenience of analysis, we assume a 3-DOF robot to be a virtual four-bar linkage ABCDA, shown in Fig. 10.18. AD is named the virtual frame (r_4); AB is called the virtual input link (r_1); BC is the virtual couple link (r_2); and CD expresses the virtual output link (r_3). For the virtual output link r_3 of the “virtual four-bar linkage” to be a crank that is capable of continuous rotation through 360° , the following Grashoff's conditions must be satisfied:

$$r_1 + r_3 \leq r_2 + r_4 \cap r_2 + r_3 \leq r_1 + r_4 \cap r_4 + r_3 \leq r_1 + r_2 \quad (r_3 \text{ is the shortest}) \quad (10.105)$$

or

$$r_1 + r_4 \leq r_2 + r_3 \cap r_2 + r_4 \leq r_1 + r_3 \cap r_3 + r_4 \leq r_1 + r_2 \quad (r_4 \text{ is the shortest}) \quad (10.106)$$

where, if r_3 is the shortest of the four links, we utilize inequalities (10.105); if r_4 is the shortest, we utilize inequalities (10.106). From Grashoff's theory, we obtain the following criterion:

If the output link r_3 is a crank, i.e., the conditions (10.105) or (10.106) are satisfied, the dextrous workspace of the 3-DOF robot exists in this position, and conversely.

By means of the criterion and the solution space, we obtain the following classes of dextrous workspace: (1) null, (2) single-loop, (3) plate, and (4) double-loop. Three of these classes are shown in Fig. 10.20.

Figure 10.21 shows the relationship between the areas of the dextrous workspaces and the link lengths of all 3-DOF planar serial mechanisms. From Figs. 10.2(b) and 10.21, we conclude the following:

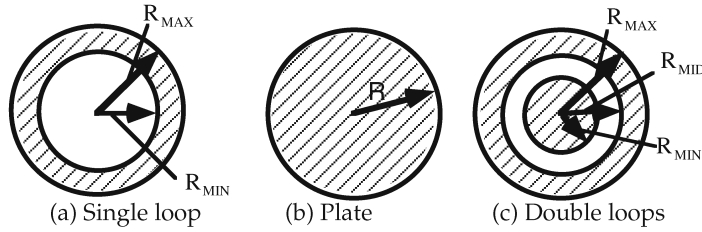


FIGURE 10.20 Classification of dextrous workspace.

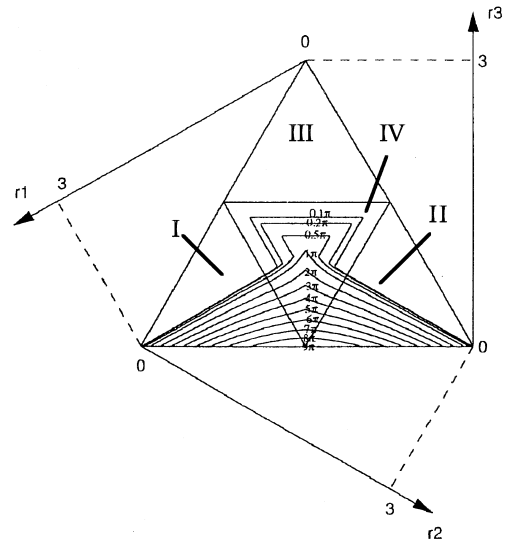


FIGURE 10.21 Dextrous workspace atlas.

- When r_3 is small and $r_1 = r_2$, the area of the dextrous workspace is large and approximately equal to 9π .
- Within regions I_2 , II_2 , and III as shown in Fig. 10.2(b), the dextrous workspaces of the robots do not exist, which are null.
- Within regions I_1 and II_1 , the dextrous workspaces of the robots are a single-loop.
- Within regions IV_1 , IV_2 , and IV_6 , the dextrous workspaces of the robots are a plate.
- When $r_1 = r_2 \cap r_3 < r_1$ (region IV_1), the robots have large dextrous workspaces. This result has important consequences for design of robots with dextrous manipulation.
- Within regions IV_3 and IV_4 , the dextrous workspaces of the robots are a double-loop.

Global Workspace Atlas

Using the results of Gosselin and Angeles [31], we derive the global workspace areas of the 3-DOF planar serial manipulator as follows:

$$A_{GW} = \int_0^{2\pi} \pi[(r_1 + r_2)^2 - (r_1 - r_2)^2] d\phi_3 = 8\pi^2 r_1 r_2 \quad (10.107)$$

The global workspace implies that when all orientations ϕ_3 of the output link r_3 are given, the end-effector can reach points in the space spanned by coordinates x, y, ϕ_3 .

By use of Eq. (10.107), contours in the global workspace of all 3-DOF planar serial manipulators can be plotted on the model of the solution space. Fig. 10.22 illustrates the relationship between the volume of the global workspace and the link lengths. We conclude the following:

- When r_3 is small and $r_1 = r_2$, the global workspace has maximum volume and is approximately equal to $18\pi^2$.
- If r_3 is specified and $r_1 = r_2$, the volume of the global workspace is large.
- The volume of the global workspace is inversely proportional to r_3 .

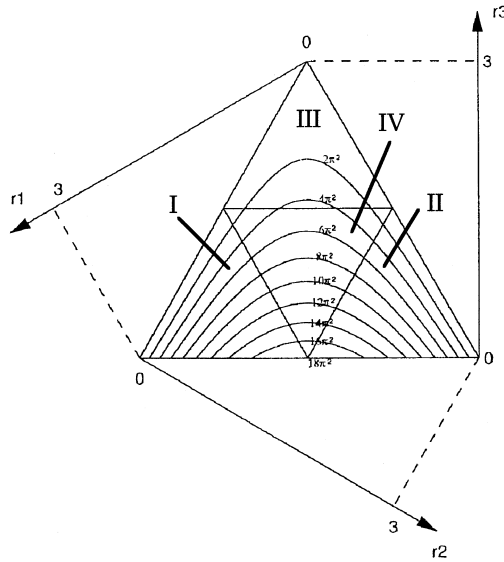


FIGURE 10.22 Global workspace atlas.

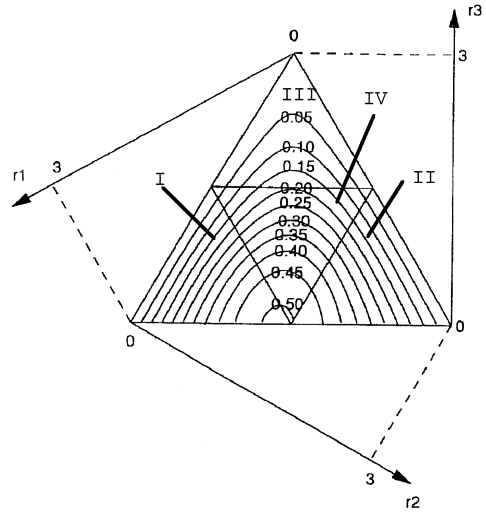


FIGURE 10.23 Atlas of global conditioning index.

Atlas of Global Conditioning Index

By using Eq. (10.59), contours in the global conditioning index of all 3-DOF planar serial manipulators can be plotted on the model of the solution space.

In particular, a large value of the index ensures that the manipulator can be precisely controlled. Fig. 10.23 describes the relationship between the global conditioning index and the link lengths of all 3-DOF planar robotic mechanisms.

From Fig. 10.23, we see that

- If r_3 is small, $r_1 \cong r_2$ and $r_1 < r_2$, the global conditioning index of the robots is large.
- The global conditioning index of mechanisms located on lines parallel to axis r_3 is inversely proportional to r_3 .

Atlases of Global Velocity Index

Using Eqs. (72) and (73), the atlases of the global maximum and minimum linear velocity indices are plotted on the solution space model of robotic mechanisms with three moving links. Figs. 10.24 and 10.25 illustrate relationships between the global maximum and minimum linear velocity indices and the link lengths of 3-DOF planar robotic mechanisms, respectively. From Figs. (10.24) and (10.25), we conclude the following:

- If $r_1 = r_2 + r_3$ and $r_1 \cong r_2$, the global maximum linear velocity index of the robots is small as shown in Fig. 10.24.
- In region IV, we obtain a large value of the global minimum linear velocity index. This result is very important for design of robots in which the end-effector should move quickly as shown in Fig. 10.25.
- In the case of serial robots, the global maximum and minimum angular velocity indices are equal and constant.

Atlases of Global Payload Index

By means of Eqs. (10.78) and (10.79), the atlases of global maximum and minimum force payload indices are constructed on the solution space model. Figs. 10.26 and 10.27 are contours of global maximum and minimum force payload indices for 3-DOF planar robotic mechanisms, respectively. And Fig. 10.28

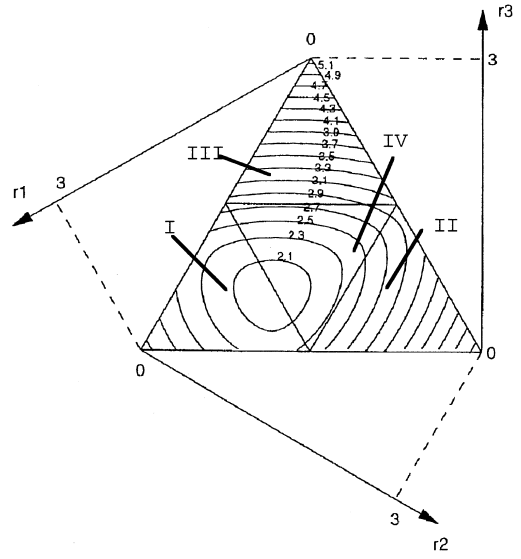


FIGURE 10.24 Atlas of global maximum linear velocity index.

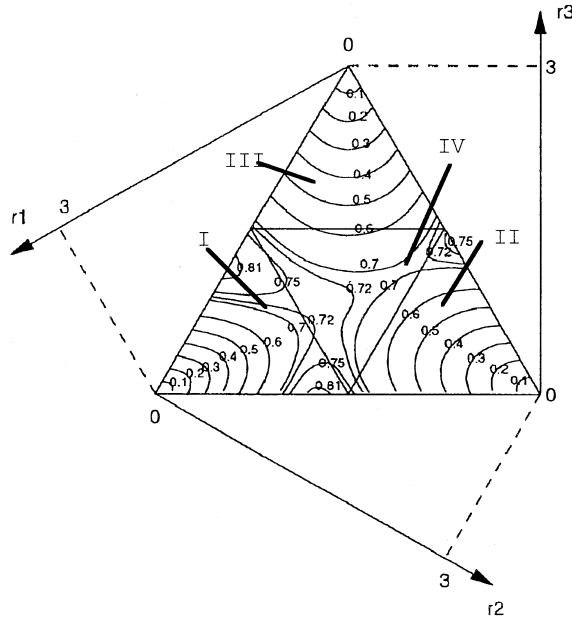


FIGURE 10.25 Atlas of global minimum linear velocity index.

describes the global maximum torque payload index. From Figs. 10.26, 10.27, and 10.28, we obtain the following:

- If r_3 is small and $r_1 = r_2$, the global maximum force payload index is small; if r_3 is given and $r_1 = r_2$, the global maximum force payload index is large, and values of the global maximum force payload index of mechanisms located on lines parallel to the axis r_3 is inversely proportional to r_3 and symmetric about the axis $r_1 = r_2$ as shown in Fig. 10.26.
- If r_3 is given and $r_1 = r_2$, the global minimum force payload index is small; the global minimum force payload index of mechanisms located on lines parallel to the axis r_3 is proportional to r_3 and symmetric about the axis $r_1 = r_2$ as shown in Fig. 10.27.

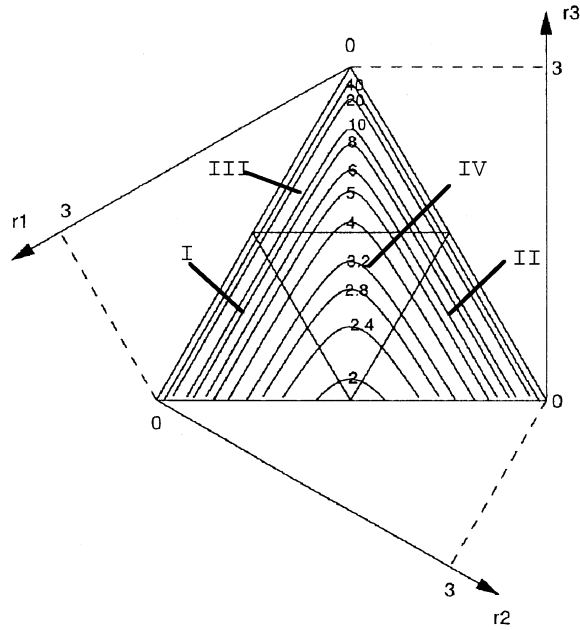


FIGURE 10.26 Atlas of global maximum force payload index.

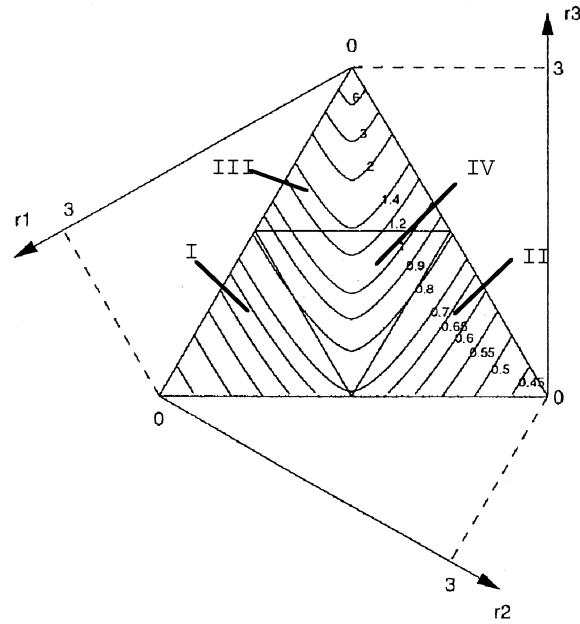


FIGURE 10.27 Atlas of global minimum force payload index.

- If r_3 is small and $r_1 = r_2$, the global maximum torque payload index is small; if r_3 is given, and $r_1 = r_2$, the global maximum torque payload index is large; and the global maximum torque payload index of the mechanisms located on lines parallel to the axis r_3 is proportional to r_3 and symmetric about the axis $r_1 = r_2$ as shown in Fig. 10.28.

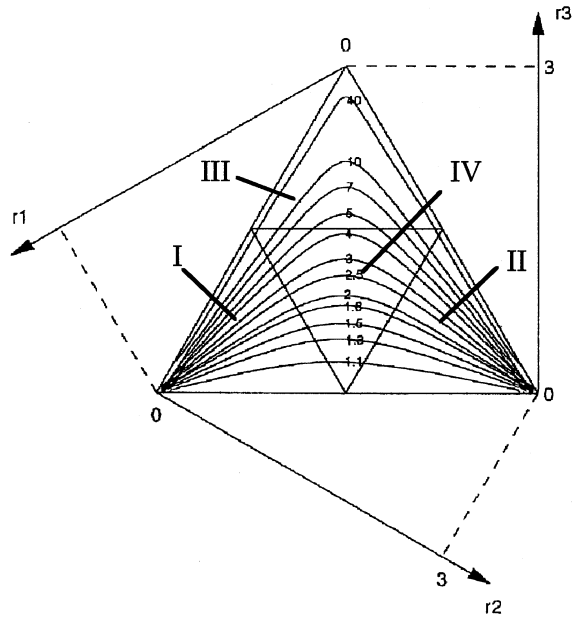


FIGURE 10.28 Atlas of global maximum torque payload index.

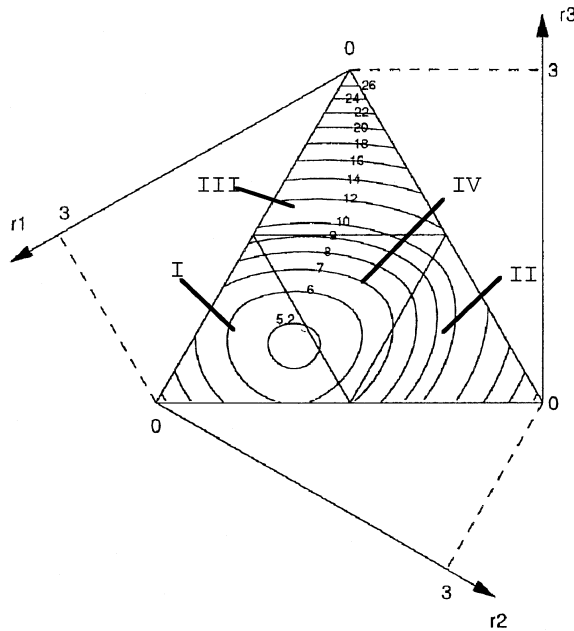


FIGURE 10.29 Atlas of global maximum position deformation index.

Atlases of Global Deformation Index

The global deformation index is a measure of stiffness of the end-effector. The global maximum and minimum deformation indices can be calculated by Eqs. (10.92) and (10.93).

Figures 10.29 and 10.30 represent contours of the global maximum and minimum position deformation indices for 3-DOF planar robotic mechanisms, respectively. Figure 10.31 represents contours

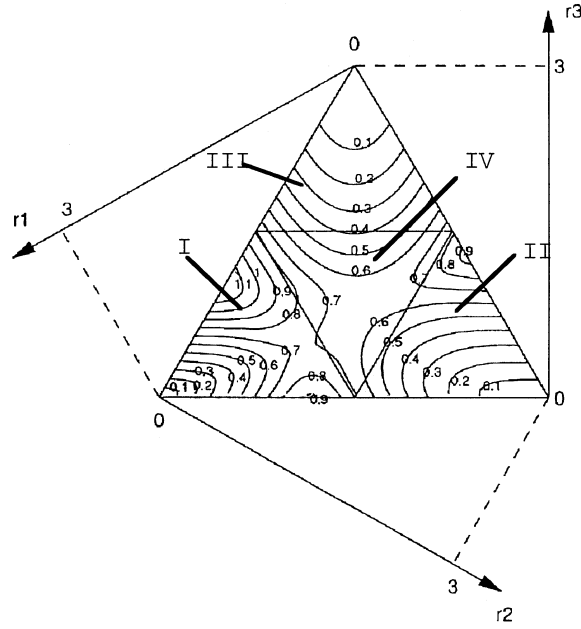


FIGURE 10.30 Atlas of global minimum position deformation index.

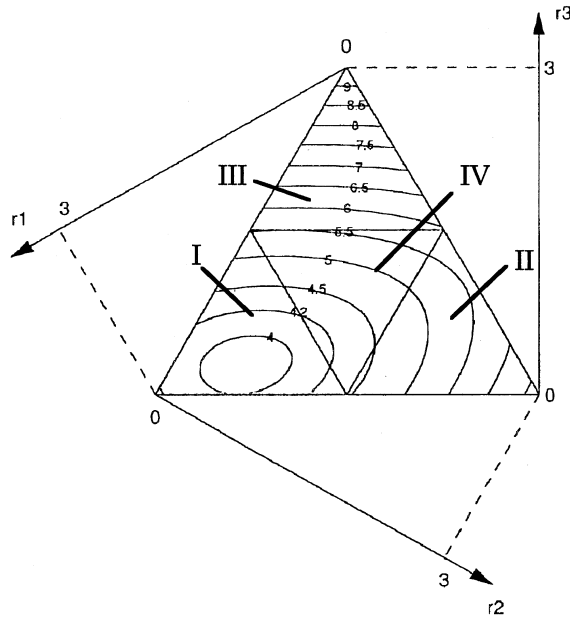


FIGURE 10.31 Atlas of global maximum orientation deformation index.

of the global maximum orientation deformation index. From Figs. 10.29, 10.30, and 10.31, we see that

- If $r_1 = r_2 + r_3$ and $r_2 \cong r_3$, the mechanisms have a small global maximum position deformation index as shown in Fig. 10.29. This result is important for robot design because we would like to reduce position deformation.
- In region IV, the global minimum position deformation index is large as shown in Fig. 10.30.

- If $r_1 > r_2 > r_3$ in region I, the global maximum orientation deformation index is small as shown in Fig. 10.31.

We have developed performance atlases for the design of serial robotic mechanisms with three moving links by plotting performance criteria on the model of the solution space. The atlases describe the relationships between the performance criteria and the link lengths of all the robotic mechanisms and can be used to design the robotic mechanisms. The technique described in this section can be utilized to analyze and design other types of robotic mechanisms.

Analysis of Commercially Available Robots

The parameters of 63 commercially available industrial and research robots are listed in Table 10.6. Figure 10.32 shows how these robots are distributed in the solution space, where each point is one of 63 industrial robot's geometric representation by link lengths. From Fig. 10.32, we see that all of the robots are located at the area ($r_1 \cong r_2$, $r_3 < r_1$ and $r_3 < r_2$) in the solution space model of three-moving-link robotic mechanisms.

The performance criteria proposed in this chapter involve kinematic and dynamic properties and characterize robot performance, which provide a basis for analyzing and designing optimum robotic mechanisms. The physical model technique, solution space model is a useful tool for investigation of the relationships between the performance criteria and link lengths of both serial and parallel robotic mechanisms. From the performance criterion atlases and an analysis of the results, we reach the following conclusions. To design optimum robotic mechanisms, we should select the robotic mechanisms with large reachable, dextrous, and global workspaces, large global conditioning index, large global minimum velocity index, large global minimum payload index, small global maximum deformation index, and small global maximum error index. For the robotic mechanisms with three moving links, the best region for selecting the dimensions of three-moving-link robots is $r_1 \cong r_2$, $r_3 < r_1$ and $r_3 < r_2$. In this region, the robotic mechanisms have optimum performance characteristics and most commercially available robots occur in the region ($r_1 \cong r_2$, $r_3 < r_1$ and $r_3 < r_2$) on the solution space model. This conclusion is very important for designing serial robotic mechanisms for use in manufacturing tasks of machine tending, assembly, and welding. The physical model technique is a useful tool for analysis and design of parallel robotic mechanisms [1,2,3,6,7,8].

10.5 Atlases for Design of F/T Sensor Based on Stewart Platform

In the design of F/T sensors, the structural design is particularly important since the sensors detect forces and moments through the measurement of strains at specific points of their bodies. Much research has been devoted to the sensor structure design. Watson [83] proposed the six-axis force sensor with three vertical deformation components. Stanford Institute [84] investigated the tube design six-axis force sensor. Schott [85] designed the double ring-shaped six-axis force sensor. Brussel [86] and Kroll [87] studied the six-axis force sensor with four vertical deformation components. Shimano [88] was the first researcher who presented and designed the cellar six-axis force sensor. Uchiyama [89] and Bayo [90] studied the systematic design procedure of the Maltese cross-bar-type force sensor. Little [91] designed the force sensor having three beams. Bicchi [82] investigated the miniaturized cylindrical force sensor for mounting on the fingertips of the dextrous hand. Diddens et al. [52] designed the ring-shaped three-axis micro force sensor for mounting in the Smartpen. Kaneko [92] proposed the twin-head type six-axis force sensor. Kerr [53] presented the Stewart-platform transducer force sensor. Nguyen [54] and Ferraresi [55] analyzed the Stewart-platform force sensor. Because the structure of the Stewart-platform force sensor is a kind of parallel mechanism, the technique for analysis and design of parallel mechanisms can be used for the design of this type of sensor.

Because it is very important to investigate the performance criteria for evaluation of the force sensors, many researchers have paid attention to this problem. Uchiyama et al. proposed an index for the evaluation of a structural isotropy of the force sensor body [93] and studied a systematic design procedure

TABLE 10.6 Dimensions of Commercial Robots

No.	Name	Original Dimensions (in mm unless specified)			Scaled Dimensions		
		R_1	R_2	R_3	r_1	r_2	r_3
1	Pentel Puha-2	315	315	0	1.5	1.5	0.0
2	Pentel Puha-1	160	100	0	1.8462	1.1538	0.0
3	Sankyo Skilam-1	400	250	0	1.8462	1.1538	0.0
4	Sankyo Skilam-2	200	160	0	1.6666	1.3333	0.0
5	Argonne Nat. Lab. E-2	18.875''	40''	5.75''	0.8762	1.8568	0.2669
6	Alpha II	177.8	177.8	129.5	1.0995	1.0995	0.8010
7	Rhino XR-3	228.6	228.6	9.5	1.4695	1.4695	0.0610
8	Intelledex 660T	304.8	304.8	228.6	1.0909	1.0909	0.8182
9	Milacron T3-756	44''	55''	1''	1.3200	1.6500	0.0300
10	Nachi-8601	1135	1500	135	1.2292	1.6246	0.1462
11	Seiko 600-5	310	310	50	1.3881	1.3881	0.2238
12	Pentel-3 GL-50	250	250	0	1.5000	1.5000	0.0
13	ABB IRB L6/2	22.5''	26''	0	1.3918	1.6082	0.0
14	Binks 88-800	39.6''	50''	0	1.3259	1.6741	0.0
15	Daewoo, NOVA-10	650	850	100	1.2187	1.5938	0.1875
16	Waseda Univ. -1	300	250	270	1.0976	9.1466	0.9878
17	Waseda Univ. -2	295	250	150	1.2734	1.0791	0.6475
18	Waseda Univ. -3	305	230	175	1.2887	0.9718	0.7395
19	Kayaba Co. Ltd.	580	410	235	1.4204	1.0041	0.5755
20	MELARM Lab.	630	550	0	1.6017	1.3983	0.0
21	Sankyo SR8437	400	400	0	1.5000	1.5000	0.0
22	Sankyo SR8438	300	250	0	1.6364	1.3636	0.0
23	Fanuc S-6	600	559.02	100	1.4297	1.3320	0.2383
24	Fanuc S-700	700	816.24	200	1.2236	1.4268	0.3496
25	Fanuc LR Mate-100	250	220	80	1.3636	1.2000	0.4364
26	Fanuc M-400	1150	780	0	1.7875	1.2124	0.0
27	Fanuc S-12	800	604.67	100	1.5950	1.2056	0.1994
28	Fanuc S-800	720	939.63	200	1.1615	1.5158	0.3227
29	Fanuc S-900	1050	1265.90	225	1.2397	1.4946	0.2657
30	Fanuc S-10	700	610	115	1.4737	1.2842	0.2421
31	Fanuc ARC Mate-100	600	559.02	100	1.4297	1.3320	0.2383
32	Fanuc ARC Mate-120	800	604.67	100	1.5950	1.2056	0.1994
33	Fanuc P-100	860	1209.34	0	1.2468	1.7532	0.0
34	Fanuc P-150	1000	1264.36	0	1.3249	1.6751	0.0
35	Fanuc S-500	900	1607.02	180	1.0048	1.7942	0.2010
36	Fanuc S-420i	950	1321.97	200	1.1529	1.6044	0.2427
37	Mitsubishi RV-M1	250	160	72	1.5560	0.9959	0.4481
38	Mitsubishi RV-M2	250	220	65	1.4019	1.2336	0.3645
39	Motoman-K10S	615	770	100	1.2424	1.5556	0.2020
40	Panasonic KS-V20	250	200	120	1.3158	1.0526	0.6316
41	Panasonic HR-50	275	275	0	1.5000	1.5000	0.0
42	Panasonic HR-150	425	425	0	1.5000	1.5000	0.0
43	Sony SRX-4 CH-LA	400	250	0	1.8462	1.1538	0.0
44	Sony SRX-4 CH-LZ	350	250	0	1.7500	1.2500	0.0
45	Stäubli RX-90	450	450	0	1.5000	1.5000	0.0
46	Stäubli RX-90L	450	650	0	1.2273	1.7727	0.0
47	Stäubli RX-130	625	625	0	1.5000	1.5000	0.0
48	Stäubli RX-130L	625	925	0	1.2097	1.7903	0.0
49	Stäubli RX-170	850	750	0	1.5938	1.4062	0.0
50	Stäubli RX-170L	850	1050	0	1.3421	1.6579	0.0
51	Seiko TT8030	400	400	40	1.4286	1.4286	0.1428
52	Seiko TT8550	225	225	0	1.5000	1.5000	0.0
53	Seiko TT8800	450	350	0	1.6875	1.3125	0.0
54	Seiko TT8010	300	200	40	1.6667	1.1111	0.2222
55	Seiko TT4000SC	356	305	0	1.6157	1.3843	0.0

TABLE 10.6 Dimensions of Commercial Robots (continued)

No.	Name	Original Dimensions (in mm unless specified)			Scaled Dimensions		
		R_1	R_2	R_3	r_1	r_2	r_3
56	Seiko TT8010C	300	200	40	1.6667	1.1111	0.2222
57	Adept-1	16.73''	14.76''	0	1.5938	1.4062	0.0
58	Adept-3	559	508	0	1.5717	1.4283	0.0
59	Adept-1850	1000	850	70	1.5625	1.3281	0.1094
60	BUAA C1 Hand	46	20	13	1.7468	0.7595	0.4937
61	IRC XDH-9S/9A Hand	50	58	0	1.3889	1.6111	0.0
62	Tokushima Univ. Hand	48	30	0	1.8462	1.1538	0.0
63	Utah DH master	39.08	43.53	11.18	1.2500	1.3924	0.0

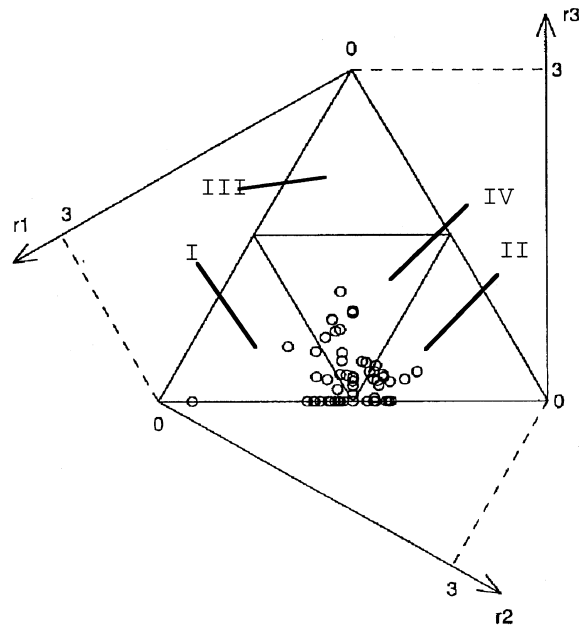


FIGURE 10.32 The distribution of commercial robots within the solution space. (a) $\theta_{AB} = 10^\circ$, (b) $\theta_{AB} = 20^\circ$, (c) $\theta_{AB} = 30^\circ$, (d) $\theta_{AB} = 40^\circ$.

to minimize a performance index for the force sensors [89]. Bayo et al [90] investigated the criteria of the condition number, stiffness, and strain gauge sensitivity of the sensors. Diddens et al [52] used a three-dimensional finite-element model to optimize the strain-gauge positions of the sensor.

Although extensive research has been directed toward the analysis and design of the structures of force sensors, there has not been an effective way to relate performance criteria and the parameters of the sensor structures. In this section, a geometric model of the solution space for the structures of the F/T sensors based on the Stewart platform is proposed and used to investigate relationships between the criteria and parameters of the structures of the F/T sensors.

Atlases of Condition Number of Jacobian Matrix

The condition number of Jacobian matrix is an important criterion for evaluation of the sensor mechanisms based on Stewart platform as shown in Fig. 10.15, since it is the measure of isotropy of a sensor.

Using the analysis approach of the parallel mechanisms, we can derive Jacobian matrix $[J]$ for the force sensor mechanisms. From Fig. 10.15, one derives

$$\sum_{i=1}^6 f_i \$i = (F) + \in (T) \quad (10.108)$$

where f_i is the force acted on the link i , and $\$i$ expresses the unit screw on the link i , i.e.,

$$\$i = (s_i) + S_{oi}, \quad (s_i)^T (s_i) = 1, \quad (s_i)^T (s_{oi}) = 0 \quad (10.109)$$

$$(s_i) = (B_i - A_i) / |B_i - A_i| \quad (10.110)$$

$$(s_{oi}) = (A_i) \times (s_i) = [(A_i) \times (B_i)] / |B_i - A_i| \quad (10.111)$$

where (A_i) and (B_i) are the coordinates of the points A_i and B_i in the coordinate system $o_A - x_A y_A z_A$. From Eq. (10.108), we can obtain

$$\begin{pmatrix} F \\ T \end{pmatrix} = [G](f) \quad (10.112)$$

where

$$(f) = (f_1 \quad f_2 \quad Pf_3 \quad f_4 \quad f_5 \quad f_6)^T$$

and

$$[G] = \begin{bmatrix} s_1 & s_2 & s_3 & s_4 & s_5 & s_6 \\ s_{o1} & s_{o2} & s_{o3} & s_{o4} & s_{o5} & s_{o6} \end{bmatrix} \quad (10.113)$$

By comparing Eq. (10.74) with Eq. (10.112), we see that Jacobian matrix $[J]$ of the mechanism has the following relationship:

$$[J] = [G]^{-1}]^T \quad (10.114)$$

So the condition number of Jacobian matrix $[J]$ can be calculated by the following equations:

$$\text{Cond} = \|J\| \|J^{-1}\|, \quad (10.115)$$

where

$$\|J\| = \sqrt{\text{tr} \left(J \frac{1}{n} [J]^T \right)} \quad (10.116)$$

Because

$$1 \leq \text{Cond} < \infty,$$

let

$$E = \frac{1}{\text{Cond}} \quad (10.117)$$

where E is the inverse of the condition number of Jacobian matrix.

By using the Eq. (10.117), the atlases of condition number can be plotted within the model of the solution space shown in Fig. 10.17. Figure 10.32 only shows four of the atlases of the condition number that can describe the relationship between the condition number and the four parameters of the sensor mechanisms.

From the atlases of the condition number as shown in Fig. 10.32, we obtain the following important result: if r_3 is small, $r_1 \cong r_2$, and both r_1 and r_2 are large; that is, in the region nearby the vertex D on the model of the solution space, the mechanisms have large values of the condition number and approximately equal to one, which means that the mechanisms in that region are isotropy. This result is very important and useful for design of the sensor mechanisms, because a large value of the condition number ensures that the force sensor can have high accuracy.

Atlases of Force and Torque Sensitivity

As shown in Fig. 10.15, from Eqs. (10.112) and (10.114), we know that the external force F and torque T applied at the upper platform center are related to the forces f_i ($i = 1, 2, \dots, 6$) by

$$\begin{pmatrix} F \\ T \end{pmatrix} = [J^T]^{-1}(f) = \begin{bmatrix} J_F \\ J_T \end{bmatrix}(f) \quad (10.118)$$

So

$$\|F\|^2 = (f)^T [J_F]^T [J_F](f) \quad (10.119)$$

$$\|T\|^2 = (f)^T [J_T]^T [J_T](f) \quad (10.120)$$

Let

$$\|f\|^2 = (f)^T(f) = 1 \quad (10.121)$$

$$L_F = (f)^T [J_F]^T [J_F](f) - \lambda_F [(f)^T(f) - 1] \quad (10.122)$$

$$L_T = (f)^T [J_T]^T [J_T](f) - \lambda_T [(f)^T(f) - 1] \quad (10.123)$$

where λ_F and λ_T are scalar Lagrange multipliers. Using the same method as that in the section entitled “Global Velocity Index,” we determine that when the force (f) (see Eq. (10.121)) is a unit vector, the maximum and minimum values of the external force F and torque T applied at the upper platform center as shown in Fig. 10.15 are

$$\|F_{\max}\| = \sqrt{\lambda_{F \max}} \quad \text{and} \quad \|F_{\min}\| = \sqrt{\lambda_{F \min}} \quad (10.124)$$

$$\|T_{\max}\| = \sqrt{\lambda_{T \max}} \quad \text{and} \quad \|T_{\min}\| = \sqrt{\lambda_{T \min}} \quad (10.125)$$

where $\|F_{\max}\|$ and $\|F_{\min}\|$ are the maximum and minimum values of the external forces, respectively; $\|T_{\max}\|$ and $\|T_{\min}\|$ express the maximum and minimum values of the external torques, respectively; and λ_F and λ_T are eigenvalues of $[J_F]^T [J_F]$ and $[J_T]^T [J_T]$, respectively.

Because we hope that the small force and torque applied at the upper platform center could make the strain gages fixed on the six links have big strain, which means that the sensor has high force and torque sensitivity, and the maximum values of the external force $\|F_{\max}\|$ and torque $\|T_{\max}\|$ should be as small as possible, we only need to consider $\|F_{\max}\|$ and $\|T_{\max}\|$.

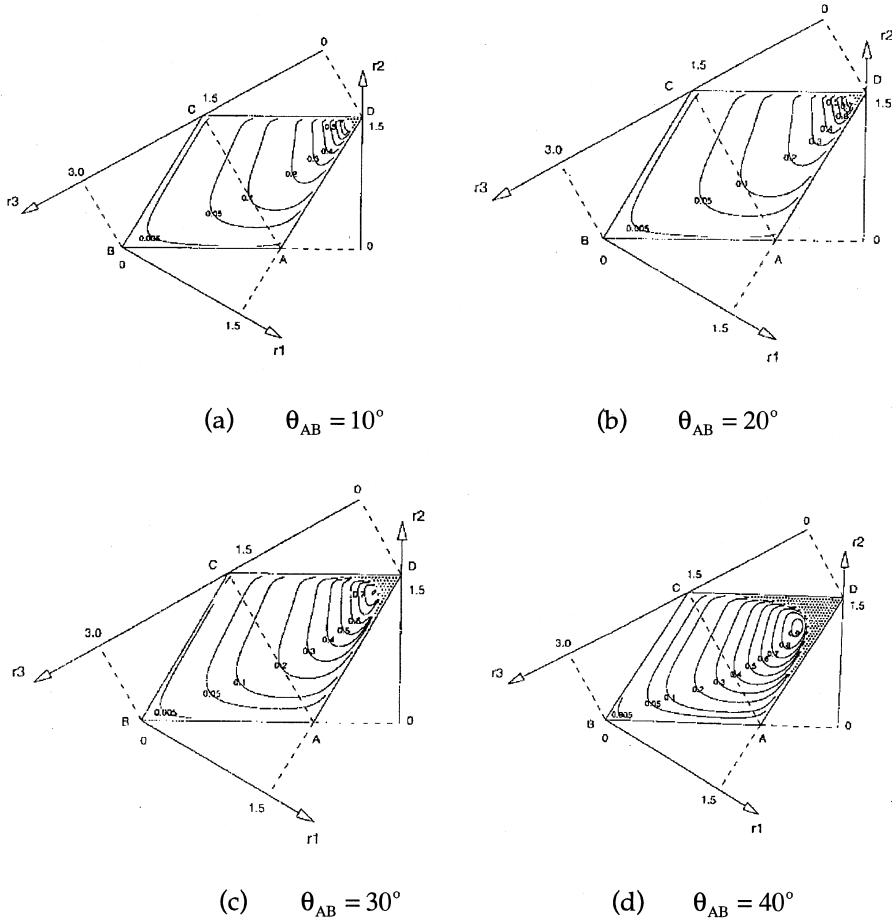


FIGURE 10.33 Four of the atlases of condition number. (a) $\theta_{AB} = 20^\circ$, (b) $\theta_{AB} = 30^\circ$, (c) $\theta_{AB} = 40^\circ$, (d) $\theta_{AB} = 50^\circ$.

By using the Eqs. (10.124) and (10.125), the atlases of the indices $\|F_{\max}\|$ and $\|T_{\max}\|$ can be plotted within the model of the solution space.

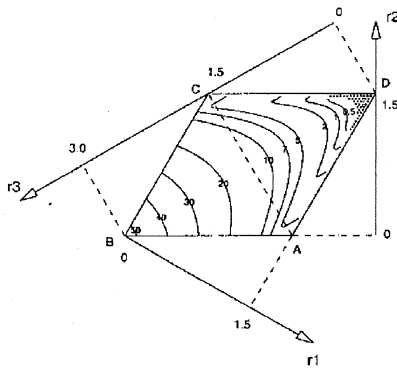
Figure 10.33 shows four of the atlases of the index $\|F_{\max}\|$, which can describe the relationship between the index $\|F_{\max}\|$ and the four parameters of the sensor mechanisms. From the atlases of the index $\|F_{\max}\|$, we obtain the following important results: if r_3 is small, ($r_1 \cong r_2$), and both r_1 and r_2 are large, that is, in the region near by the vertex D on the model of the solution space, the sensor mechanisms have small values of the index $\|F_{\max}\|$, which means that the force sensitivity of the sensors in this region is high.

Figure 10.34 shows four of the atlases of the index $\|T_{\max}\|$, which can describe the relationship between the index $\|T_{\max}\|$ and the four parameters of the sensor mechanisms. From the atlases of the index $\|T_{\max}\|$, we see that when the sensor mechanisms are located at the region near by the edges AB , AD , and CD , the sensor mechanisms have small value of the index $\|T_{\max}\|$, which means that the sensors in the region have high torque sensitivity.

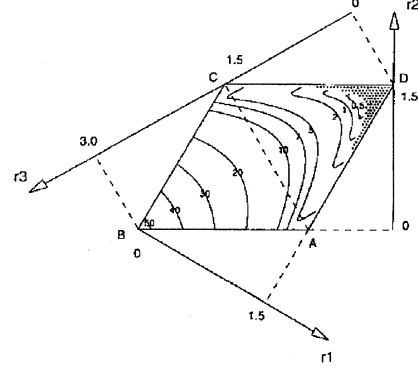
Atlases of Sensor Stiffness

Since the deformations of the upper platform of the sensor mechanism can describe the stiffness of the sensor, we need to investigate the deformations. The force (f) is related to the deformation by, as shown in Fig. 10.15,

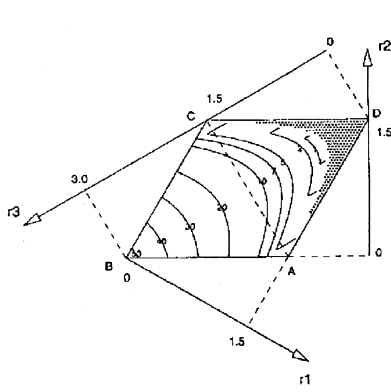
$$(f) = [K](\Delta q) \quad (10.126)$$



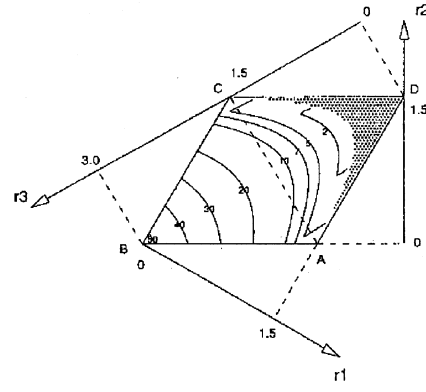
(a) $\theta_{AB} = 20^\circ$



(b) $\theta_{AB} = 30^\circ$



(c) $\theta_{AB} = 40^\circ$



(d) $\theta_{AB} = 50^\circ$

FIGURE 10.34 Four of the atlases of the index $\|F_{\max}\|$. (a) $\theta_{AB} = 10^\circ$, (b) $\theta_{AB} = 30^\circ$, (c) $\theta_{AB} = 40^\circ$, (d) $\theta_{AB} = 50^\circ$.

where

$$[K] = [I](k_1 \quad k_2 \cdots k_6)^T \quad (10.127)$$

$$(\Delta q) = (\Delta q_1 \quad \Delta q_2 \cdots \Delta q_6)^T \quad (10.128)$$

Here, Δq_i is the deformation of link i , which is connected with both upper platform and lower platform; k_i is the stiffness of link i ($i = 1, 2, \dots, 6$); and $[I]$ is a 6×6 identity matrix. We assume

$$k_i = k, \quad (10.129)$$

which implies that all six links have the same stiffness. Because of attention paid to investigation of the relationship between the stiffness and the four parameters of the sensor mechanisms, we suppose $k = 1$. From Eqs. (10.85) to (10.89), we obtain

$$(D) = \begin{pmatrix} D_p \\ D_o \end{pmatrix} = [C] \begin{pmatrix} F \\ T \end{pmatrix} = \begin{bmatrix} C_p \\ C_o \end{bmatrix} \begin{pmatrix} F \\ T \end{pmatrix} \quad (10.130)$$

where (D_p) and (D_o) express the positional deformation and orientational deformation of the upper platform, respectively.

Let

$$\|(F T)^T\|^2 = (F T)^T (F T) = 1 \quad (10.131)$$

$$L_p = (F T)[C_p]^T [C_p](F T)^T - \lambda_p [(F T)^T (F T) - 1] \quad (10.132)$$

$$L_o = (F T)[C_o]^T [C_o](F T)^T - \lambda_o [(F T)^T (F T) - 1] \quad (10.133)$$

where λ_p and λ_o are scalar Lagrange multipliers. As previously, from Eqs. (10.132) and (10.133), necessary conditions for extreme values of the positional and orientational deformations of the upper platform are

$$\|D_{p \max}\| = \sqrt{\lambda_{D_p \max}}, \quad \text{and} \quad \|D_{p \min}\| = \sqrt{\lambda_{D_p \min}}, \quad (10.134)$$

$$\|D_{o \max}\| = \sqrt{\lambda_{D_o \max}}, \quad \text{and} \quad \|D_{o \min}\| = \sqrt{\lambda_{D_o \min}}, \quad (10.135)$$

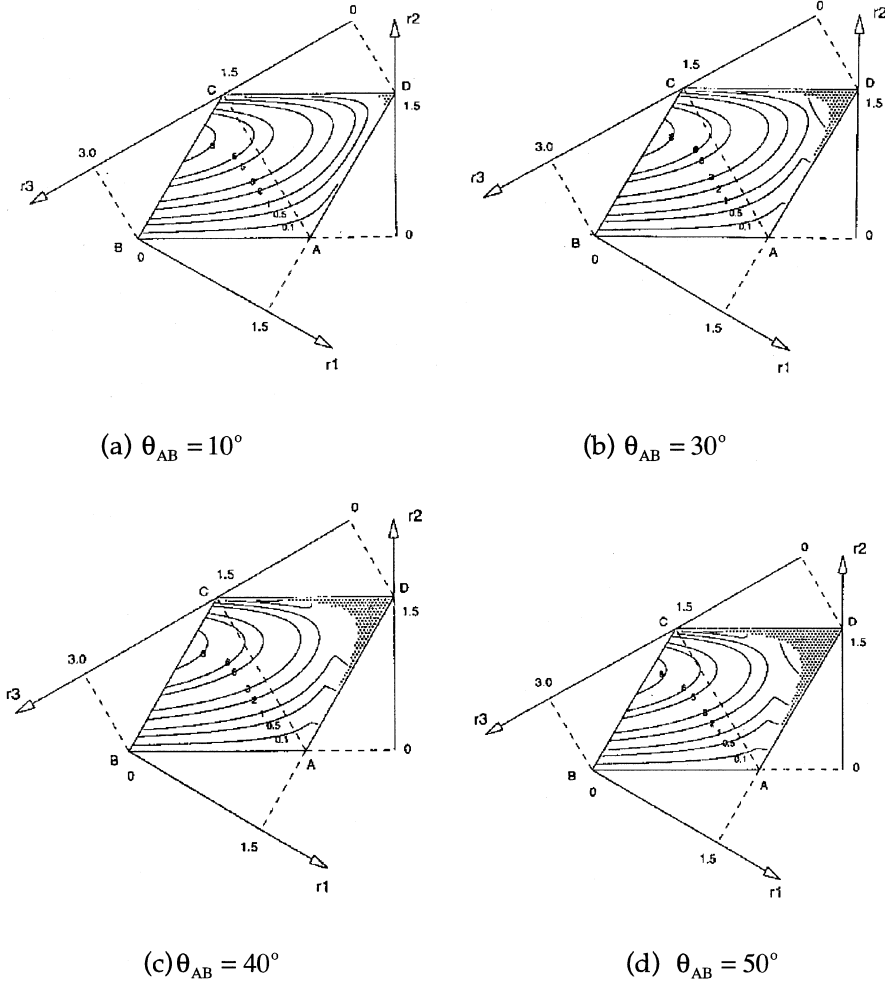


FIGURE 10.35 Four of the atlases of the index $\|T_{\max}\|$. (a) $\theta_{AB} = 30^\circ$, (b) $\theta_{AB} = 40^\circ$, (c) $\theta_{AB} = 50^\circ$, (d) $\theta_{AB} = 60^\circ$.

where, $\lambda_{D_P \max}$ and $\lambda_{D_P \min}$ are maximum and minimum eigenvalues of $[C_P]^T[C_P]$, respectively; $\lambda_{D_O \max}$ and $\lambda_{D_O \min}$ are maximum and minimum eigenvalues of $[C_O]^T[C_O]$, respectively; $\|D_P \max\|$ and $\|D_P \min\|$ are the maximum and minimum values of the positional deformations of the upper platform, respectively; and $\|D_O \max\|$ and $\|D_O \min\|$ express the maximum and minimum values of the orientational deformations of the upper platform, respectively.

Because we hope that when the force F and torque T are applied at the upper platform center, the positional and orientational deformations of the upper platform are small at the same time, which means that the sensor has high stiffness and the maximum values of the positional and orientational deformations should be as small as possible, we only need to consider $\|D_P \max\|$ and $\|D_O \max\|$.

By using the Eqs. (10.134) and (10.135), the atlases of the indices $\|D_P \max\|$ and $\|D_O \max\|$ can be plotted within the model of the solution space shown in Fig. 17.

Figure 10.35 and 10.36 show four of the atlases of the indices $\|D_P \max\|$ and $\|D_O \max\|$, respectively, which can describe the relationship between the indices $\|D_P \max\|$ and $\|D_O \max\|$ and the four parameters of the sensor mechanisms. From the atlases of the index $\|D_P \max\|$, we see that if r_3 is small, $r_1 \cong r_2$, and both r_1 and r_2 are large, that is, in the region near by the vertex D on the model of the solution space, the sensor mechanisms have small values of the index $\|D_P \max\|$ and $\|D_O \max\|$ at the sametime,

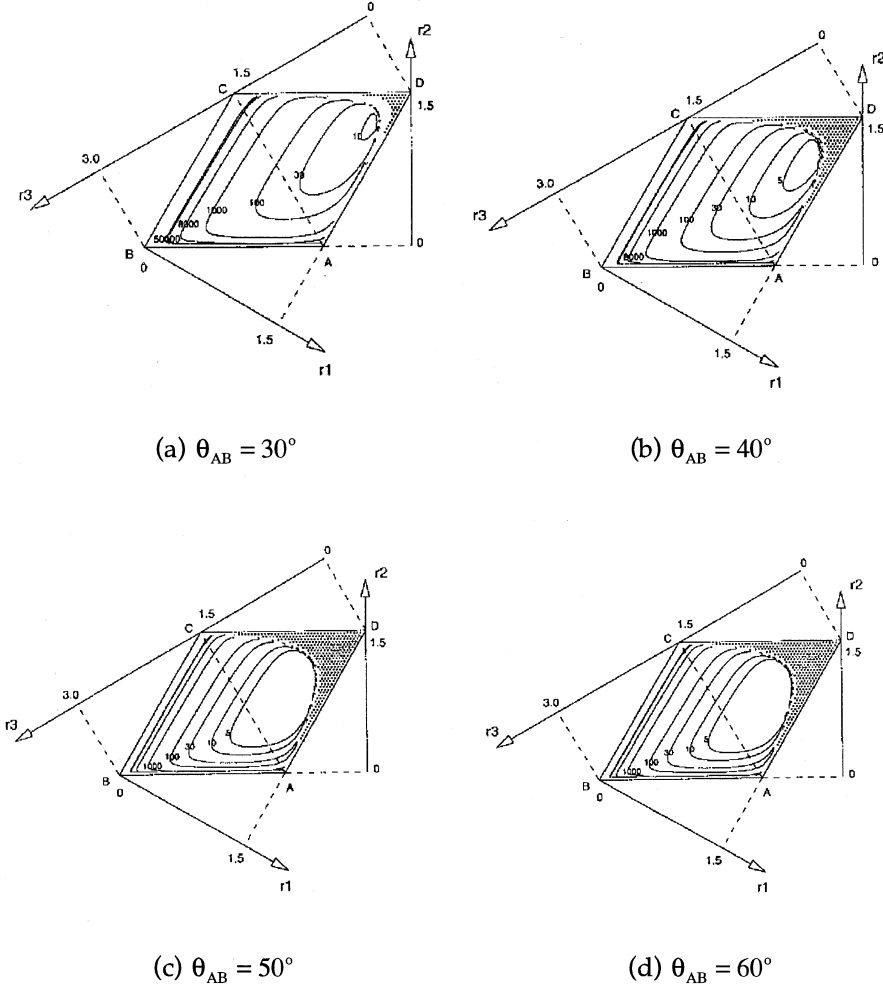


FIGURE 10.36 Four of the atlases of the index $\|D_P \max\|$. (a) $\theta_{AB} = 30^\circ$, (b) $\theta_{AB} = 40^\circ$, (c) $\theta_{AB} = 50^\circ$, (d) $\theta_{AB} = 60^\circ$.

which means that the positional and orientational stiffness of the sensors with the mechanisms are high in this region.

Sensor Design

By using the performance atlases as shown in Figs. 10.31 through 10.36, the four parameters R_1 , R_2 , R_3 , and θ_{AB} of the sensor mechanisms can be easily selected to optimize sensor performance. From the performance atlases, we see that when r_3 is small, $r_1 \cong r_2$, and both r_1 and r_2 are large, that is, in the region near by the vertex D on the model of the solution space, the sensor mechanisms have optimum performances.

Figure 10.37 is the CAD layout of sensor mechanism. Because we hope to make the sensor as small as possible, the elastic joints are utilized to replace the spherical joints as shown in Fig. 10.38, which makes it possible to manufacture the small size sensors.

To use the model of the solution space for design of the F/T sensor mechanisms based on Stewart platform is a novel and useful method for investigation of the optimal sensor design. The three kinds of atlases of the criteria, including condition number, force and torque sensitivity, and stiffness of the sensors clearly show relationships between the performance criteria and parameters of all the sensor mechanisms. By using the performance atlases, an optimal design for the sensor mechanism can be achieved. Because

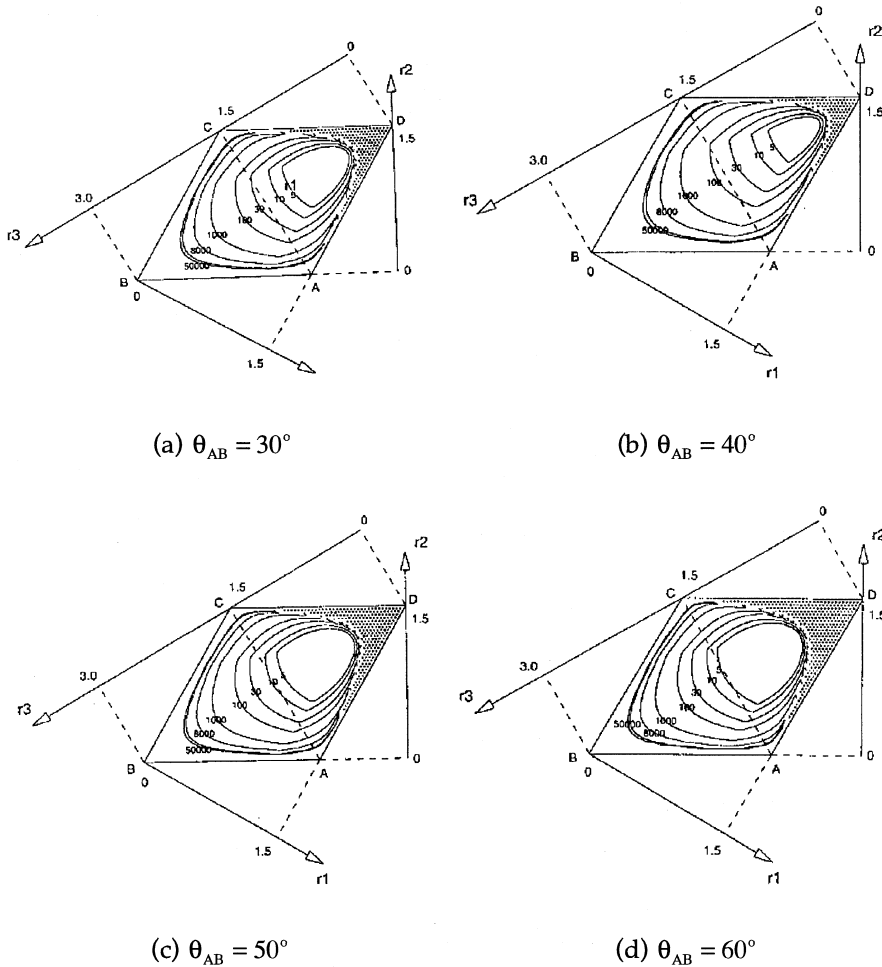


FIGURE 10.37 Four of the atlases of the index $\|D_{O \max}\|$.

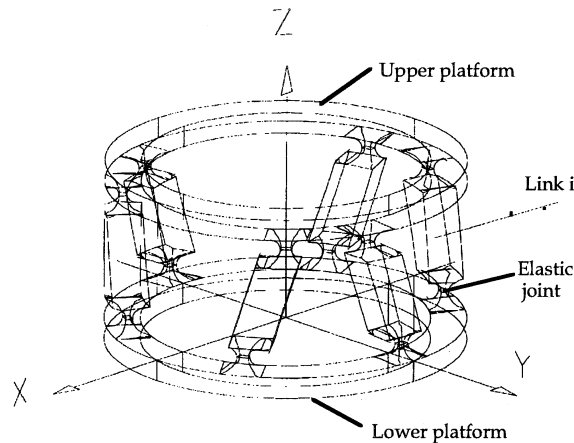


FIGURE 10.38 CAD layout of sensor house.

the elastic joints were proposed for replacing the spherical joints, the Stewart-based sensor can be designed as small as possible.

10.6 Conclusions

The physical model technique is a simple, useful, and efficient tool for design of robotic manipulators. By using the technique and the performance criteria, the relationships between the criteria and dimensions of robotic mechanisms can be obtained as the performance atlases, which are easily utilized for optimal robotic design.

References

1. F. Gao, X. Q. Zhang, Y. S. Zhao, and W. B. Zu, "Distribution of some properties in a physical model of the solution space of 2-DOF parallel planar manipulators," *Mechanism and Machine Theory*, Vol. 30, No. 6, 1995, pp. 811–817.
2. F. Gao, X. Q. Zhang, Y. S. Zhao, and H. R. Wang, "A physical model of the solution space and the atlases of the reachable workspaces for 2-DOF parallel planar manipulators," *Mechanism and Machine Theory*, Vol. 31, No. 2, 1996, pp. 173–184.
3. F. Gao, Y. S. Zhao, and Z. H. Zhang, "Physical model of the solution space of 3-DOF parallel planar manipulators," *Mechanism and Machine Theory*, Vol. 31, No. 2, 1996, pp. 161–171.
4. F. Gao, W. A. Gruver, and Y. Zhang, "Performance charts for design of robotic mechanisms with three moving links," *IEEE SMC96*, Oct. 14–17, 1996, Beijing, China.
5. F. Gao and W. A. Gruver, "Performance Evaluation Criteria for Analysis and Design of Robotic Mechanisms," *IEEE CIRA'97*, July 1997, Monterey, California.
6. F. Gao and W. A. Gruver, "The global conditioning index in the solution space of two degrees of freedom planar parallel manipulators," *Proc. of the 1995 IEEE International Conference on SMC*, October 1995, Vancouver, Canada, Vol. 5, pp. 4055–4059.
7. F. Gao, X. J. Liu, and W. A. Gruver, "Performance Evaluation of Two Degree of Freedom Planar Parallel Robots," accepted for publication in *Mechanism and Machine Theory*, 1997.
8. F. Gao, W. A. Gruver, et al., "A geometric model for the analysis and design of Delta parallel robots," *ASME Design Engineering Technical Conferences and Computers in Engineering Conference*, August 18–22, 1996, Irvine, California.
9. F. Gao and W. A. Gruver, "Criteria based analysis and design of three degree of freedom planar robotic manipulators," *IEEE ICRA'97*, April 20–25, 1997, Albuquerque, New Mexico.

10. F. Skinner, "Designing a multiple pretension manipulator," *Mechanical Engineering*, September 1975, pp 30–37.
11. F. R. E. Crossley and F. G. Umholtz, "Design for a three-fingered hand," *Mechanism and Machine Theory*, Vol. 12, 1977, pp 85–93.
12. A. Rovetta, P. Vincentini, and I. Franchetti, "On development and realization of a multipurpose grasping system," *Proc. of the 11th International Symposium on Industrial Robots*, Tokyo, 1981, pp 273–280.
13. T. Okada, "Computer control of multi-jointed finger system for precise object-handling," *IEEE Transactions on Systems, Man and Cybernetics*, Vol. SMC-12 (3), 1982, pp 289–299.
14. J. K. Salisbury, "Kinematic and force analysis of articulated hands," Ph.D. Thesis, Stanford University, 1982, Report No. STAN-CS-82-921.
15. S. C. Jacobsen, J. E. Wood, D. F. Knutti, and K. B. Biggers, "The Utah/MIT dextrous hand: work in progress," *The International Journal of Robotics Research*, 1984, Vol. 3, No. 4, pp 21–50.
16. P. Dario and G. Buttazzo, "An anthropomorphic robot finger for investigating artificial tactile perception," *The International Journal of Robotics Research*, 1987, Vol. 6, No. 3, pp 25–48.
17. B. A. Grupen, T. C. Henderson, and I. D. McCammon, "A survey of general-purpose manipulation," *The International Journal of Robotics Research*, 1989, Vol. 8, No. 1, pp 38–62.
18. S. A. Stansfield, "Robotic grasping of unknown objects: a knowledge-based approach," *The International Journal of Robotics Research*, 1991, Vol. 10, No. 4, pp 314–326.
19. K. H. Hunt, A. E. Samuel, and P. R. McAre, "Special configurations of multi-finger multi-freedom grippers—a kinematic study," *The International Journal of Robotics Research*, 1991, Vol. 10, No. 2, pp 123–134.
20. R. N. Rohling and J. M. Hollerbach, "Modeling and parameter estimation of the human index finger," *Proc. of the IEEE International Conference on Robotics and Automation*, 1994, pp 223–230.
21. Y. Yang, Y. Zhang, and Q. X. Zhang, "A performance evaluation of HB-2 dextrous robotic hand," *Proc. of the IEEE International Conference on Systems, Man and Cybernetics*, 1995, Vancouver, Vol. 1, pp 922–927.
22. P. R. McAre, A. E. Samuel, K. H. Hunt, and C. G. Gibson, "A dexterity measure for the kinematic control of a multifinger, multifreedom robot hand," *The International Journal of Robotics Research*, 1991, Vol. 10, No. 5, pp 439–453.
23. T. Yoshikawa, "Manipulability of robotic mechanism," *The International Journal of Robotics Research*, 1985, Vol. 4, No. 2, pp 3–9.
24. T. W. Nye, D. J. LeBlanc, and R. J. Cipra, "Design and modeling of a computer-controlled planar manipulator," *The International Journal of Robotics Research*, 1987, Vol. 6, No. 1, pp 85–95.
25. C. J. J. Paredis and P. K. Khosla, "Kinematic design of serial link manipulators from task specifications," *The International Journal of Robotics Research*, 1993, Vol. 12, No. 3, pp 274–287.
26. D. Tesar and M. S. Butler, "A generalized modular architecture for robot structures," *Manufacturing Review*, 1989, Vol. 2, No. 2, pp 91–118.
27. D. Tesar and M. Sklar, "Dynamic analysis of hybrid serial manipulator systems parallel modules," *ASME Trans. Journal of Mechanisms, Transmission, and Automation in Design*, 1988, Vol. 104, pp 218–228.
28. P. Gorce, O. Vanel, and C. Ribreau, "Equilibrium study of 'human' robot," *Proc. of the IEEE International Conference on Systems, Man and Cybernetics*, 1995, Vancouver, Vol. 2, pp 1309–1314.
29. T. A. McMahon, "Mechanics of locomotion," *The International Journal of Robotics Research*, 1984, Vol. 3, No. 2, pp 4–28.
30. S. Hirose and O. Kunieda, "Generalized standard foot trajectory for a quadruped walking vehicle," *The International Journal of Robotics Research*, 1991, Vol. 10, No. 1, pp 3–12.
31. C. Gosselin and J. Angeles, "The optimum design of planar three-degree-of-freedom parallel manipulator," *ASME Journal of Mechanisms, Transmissions, and Automation in Design*, Vol. 110, No. 1, 1988, pp. 35–41.
32. R. J. Schilling, *Fundamentals of Robotics Analysis and Control*, Prentice-Hall, Inc., 1990.

33. C. Y. Ho and J. Sriwattanathamma, *Robot Kinematics: Symbolic Automation and Numerical Synthesis*, Ablex Publishing Corporation, 1989.
34. R. E. Parkin, *Applied Robotic Analysis*, Prentice-Hall, Inc., 1991.
35. H. Asada and Y. T. Kamal, *Direct-Drive Robots Theory and Practice*, MIT Press, 1987.
36. C. M. Gosselin and M. Guillot, "The synthesis of manipulators with prescribed workspaces," *Trans. of ASME, J. of Mechanical Design*, Vol. 113, 1991, pp. 451–455.
37. D. McCloy, "Some comparisons of serial driven and parallel driven manipulators," *Robotica*, Vol. 8, 1990, pp. 355–362.
38. D. McCloy, "Planar linkages for parallel-driven manipulators," *The 4th Conference of the Irish Manufacturing Committee*, Limerick, Ireland, 1987.
39. A. Bajpai and B. Roth, "Workspace and mobility of a closed loop manipulator," *International J. Robotics Research*, No. 2, 1986, pp. 131–142.
40. H. Asada and K. Youcef-Toumi, "Analysis and design of a direct drive arm with a five-bar link parallel driven mechanism," *Proc. of the American Control Conference*, San Diego, 1984.
41. R. Stoughton and T. Kokkinia, "Some properties of a new kinematic structure for robot manipulators," *ASME Design Automation Conference*, DET-Vol. 10-2, 1987, pp. 73–79.
42. V. Kumar, "Characterization of workspaces of parallel manipulators," *ASME J. Mechanical Design*, Vol. 114, 1992, pp. 368–375.
43. C. Gosselin and J. Angeles, "A global performance index for the kinematic optimization of robotic manipulators," *Trans. ASME, J. of Mechanical Design*, Vol. 113, 1991, pp. 220–226.
44. F. Sternheim, "Computation of the direct and inverse geometric models of the DELTA4 parallel robot," *Robotersysteme*, Vol. 3, 1987, pp. 199–203.
45. F. Sternheim, "Tridimensional computer simulation of parallel robot. Results for the DELTA4 machine," *Proc. of the 18th International Symposium on Industrial Robots*, Lausanne, 1988.
46. R. Clavel, "DELTA, a fast robot with parallel geometry," *Proc. of the 18th Int. Symposium on industrial Robots*, IFS Publications, 1988, pp. 91–100.
47. K. Miller and R. Clavel, "The Lagrange-based model of Delta-4 robot dynamics," *Robotersysteme*, Vol. 8, 1992, pp. 49–54.
48. F. Pierrot, A. Fournier, and P. Dauchez, "Toward a fully parallel 6-DOF robot for high-speed applications," *International Journal of Robotics and Automation*, Vol. 7, No. 1, 1992, pp. 15–22.
49. F. Pierrot, C. Reynaud, and A. Fournier, "DELTA: a simple and efficient parallel robot," *Robotica*, Vol. 8, 1990, pp. 105–109.
50. F. Pierrot and A. Fournier, "Fast models for the DELTA parallel robot," *Proc. of I.F.I.P.*, Rome, Italy, 1990, pp. 123–130.
51. E. O. Doebelin, *Measurement systems applications and design*, McGraw Hill, New York, 1985.
52. D. Diddens, D. Reynaerts, and H. V. Brussel, "Design of a ring-shaped three-axis micro force/torque sensor," *Sensors and Actuators A*, 46–47, 1995, pp. 225–232.
53. D. R. Kerr, "Analysis, properties and design of a Stewart-platform transducer," *J. Mech. Transm. Autom. design*, Vol. 111, 1989, pp. 25–28.
54. C. C. Nguyen, S. S. Antrazi, Z.-L. Zhou, and C. E. Campbell, Jr., "Analysis and experimentation of a Stewart platform-based force/torque sensor," *International Journal of Robotics and Automation*, Vol. 7, No. 3, 19, pp. 133–140.
55. C. Ferraresi, S. Pastorelli, M. Sorli, and N. Zhmud, "Static and dynamic behavior of a high stiffness Stewart platform-based force/torque sensor," *Journal of Robotic Systems*, Vol. 12, No. 12, 1995, pp. 883–893.
56. K. C. Gupta and B. Roth, "Design considerations for manipulator workspace," *Trans. ASME, Journal of Mechanical Design*, Vol. 104, 1982, pp. 704–711.
57. J. K. Davidson, "A synthesis procedure for design of 3-R planar robotic workcells in which large rotations are required at the workpiece," *Journal of Mechanical Design*, Vol. 114, 1992, pp. 547–558.
58. C. D. Lin and F. Freudenstein, "Optimization of the workspace of a three-link turning-pair connected robot arm," *The International Journal of Robotics Research*, Vol. 5, No. 2, 1986, pp. 104–111.

59. C. M. Gosselin and M. Jean, "Determination of the workspace of planar parallel manipulators with joint limits," *Robotics and Autonomous Systems*, Vol. 17, 1996, pp. 129–138.
60. V. Kumar, "Characterization of workspaces of parallel manipulators," *Trans. ASME, Journal of Mechanical Design*, Vol. 114, 1992, pp. 368–375.
61. A. Bajpai and B. Roth, "Workspace and mobility of a closed-loop manipulator," *The International Journal of Robotics Research*, Vol. 5, No. 2, 1986, pp. 131–142.
62. M. Trabia and J. K. Davidson, "Design conditions for the orientation and attitude of a robot tool carried by a 3-R spherical wrist," *Trans. ASME, Journal of Mechanisms Transmissions, and Automation in Design*, Vol. 111, 1989, pp. 176–186.
63. G. R. Pennock and D. J. Kassner, "The workspace of a general geometry planar three-degree-of-freedom platform-type manipulator," *Trans. ASME, Journal of Mechanical Design*, Vol. 115, 1993, pp. 269–276.
64. C. Gosselin, "Determination of the workspace of 6-DOF parallel manipulators," *Trans. ASME, Journal of Mechanical Design*, Vol. 112, 1990, pp. 331–336.
65. J. Angeles and C. S. Lopez-Cajun, "Kinematic isotropy and the conditioning index of serial robotic manipulators," *The International Journal of Robotics Research*, Vol. 11, No. 6, 1992, pp. 560–571.
66. J. Angeles, "The Design of Isotropic manipulator architectures in the presence of redundancies," *The International Journal of Robotics Research*, Vol. 11, No. 3, 1992, pp. 196–201.
67. C. A. Klein, "Spatial robotic isotropy," *The International Journal of Robotics Research*, Vol. 10, No. 4, 1991, pp. 426–437.
68. M. Kircanski, "Kinematic isotropy and optimal kinematic design of planar manipulators and a 3-DOF spatial manipulator," *The International Journal of Robotics Research*, Vol. 15, No. 1, 1996, pp. 61–77.
69. C. M. Gosselin, "The optimum design of robotic manipulators using dexterity indices," *Robotics and Autonomous System*, Vol. 9, 1992, pp. 213–226.
70. C. A. Klein and B. E. Blaho, "Dexterity measures for the design and control of kinematically redundant manipulators," *The International Journal of Robotics Research*, Vol. 6, No. 2, 1987, pp. 72–83.
71. F. C. Park and R. W. Brockett, "Kinematic dexterity of robotic mechanisms," *The International Journal of Robotics Research*, Vol. 13, No. 1, 1994, pp. 1–15.
72. P. R. McAre, A. E. Samuel, K. H. Hunt, and C. G. Gibson, "A dexterity measure for the kinematic control of a multifinger, multifreedom robot hand," *The International Journal of Robotics Research*, Vol. 10, No. 5, 1991, pp. 439–453.
73. T. Yoshikawa, "Manipulability of robotic mechanisms," *The International Journal of Robotics Research*, Vol. 4, No. 2, 1985, pp. 3–9.
74. J. P. Merlet, "Singular configurations of parallel manipulators and Grassmann geometry," *The International Journal of Robotics Research*, Vol. 8, No. 5, 1989, pp. 45–56.
75. J. Sefrioui and C. M. Gosselin, "Singularity analysis and representation of planar parallel manipulators," *Robotics and Autonomous Systems*, Vol. 10, 1992, pp. 209–224.
76. D. K. Pai, "Genericity and singularities of robot manipulators," *IEEE Transactions on Robotics and Automation*, Vol. 8, No. 5, 1992, pp. 545–595.
77. C. J. J. Paredis and P. K. Khosla, "Kinematic design of serial link manipulators from task specifications," *The International Journal of Robotics Research*, Vol. 12, No. 3, 1993, pp. 274–287.
78. K. V. D. Doel and D. K. Pai, "Performance measures for robot manipulators: a unified approach," *The International Journal of Robotics Research*, Vol. 15, No. 1, 1996, pp. 92–111.
79. C. Gosselin and J. Angeles, "The optimum kinematic design of a spherical three-degree-of-freedom parallel manipulator," *Trans. ASME, Journal of Mechanisms Transmissions, and Automation in Design*, Vol. 111, 1989, pp. 202–207.
80. C. Gosselin and J. Angeles, "Kinematic inversion of parallel manipulators in the presence of incompletely specified tasks," *Trans. ASME, Journal of Mechanical Design*, Vol. 112, 1990, pp. 494–500.

81. C. Gosselin and E. Lavoie, "On the kinematic design of spherical three-degree-of-freedom parallel manipulators," *The International Journal of Robotics Research*, Vol. 12, No. 4, 1993, pp. 394–402.
82. A. Bicchi, "A criterion for optimal design of multi-axis force sensors," *Robotics and Autonomous Systems*, Vol. 10, No. 4, 1992, pp. 269–286.
83. P. C. Watson and S. H. Drake, "Pedestal and wrist force sensors for automatic assembly," *Proc. the 5th Int. Symp. on Industrial Robots*, 1975, pp. 501–511.
84. "Robot Technology," Kogon Page Ltd., London, 1983.
85. J. Schott, "Tactile sensor with decentralized signal conditioning," *The 9th IMEKO World Congress*, Beilin, 1982.
86. H. V. Brussel, et al., "Force sensing for advanced robot control," *Proc. of the 5th Int. Cof. on Robot Vision and Sensory Controls*, 1980.
87. E. Kroll, et al., "Decoupling load components and improving robot interfacing with an easy-to-use 6-axis wrist force sensor," *Theory of Machines and Mechanisms*, *Proc. of the 7th World Congress*, 1986.
88. B. Shimano, et al., "On force sensing information and its use in controlling manipulators," *Proc. of the 8th Int. Symp. on Industrial Robots*, 1979.
89. M. Uchiyama, E. Bayo, and E. Palma-Villalon, "A systematic design procedure to minimize a performance index for robot force sensors," *Trans. ASME, Journal of Dynamic Systems, Measurement, and Control*, Vol. 113, 1991, pp. 388–394.
90. E. Bayo and J. R. Stubbe, "Six-axis force sensor evaluation and a new type of optimal frame truss design for robotic applications," *Journal of Robotic Systems*, Vol. 6, No. 2, 1989, pp. 191–208.
91. R. Little, "Force/Torque sensing in robotic manufacturing," *Sensors, The Journal of Machine Perception*, Vol. 9, No. 11, 1992.
92. M. Kaneko, "Twin-head six-axis force sensors," *IEEE Transactions on Robotics and Automation*, Vol. 12, No. 1, 1996, pp. 146–154.
93. M. Uchiyama, Y. Nakamura, and K. Hakomori, "Evaluation of robot force sensor structure using singular value decomposition," *Journal of the Robotics Society of Japan*, Vol. 5, No. 1, 1987, pp. 4–10.